Simulations of Turbulent Flows with Strong Shocks and Density Variations: Final Report

Work supported under grant number DE-FC02-06-ER25787 from the Department of Energy under the SciDAC II program

Sanjiva K. Lele (P.I.)

Stanford University

<lele@stanford.edu>

http://shocks.stanford.edu

October 1, 2012

Contents

1 Project Overview

The target of this SciDAC Science Application was to develop a new capability based on high-order and high-resolution schemes to simulate shock-turbulence interactions and multi-material mixing in planar and spherical geometries, and to study Rayleigh-Taylor and Richtmyer-Meshkov turbulent mixing. These fundamental problems have direct application in high-speed engineering flows, such as inertial confinement fusion (ICF) capsule implosions and scramjet combustion, and also in the natural occurrence of supernovae explosions.

Another component of this project was the development of subgrid-scale (SGS) models for large-eddy simulations of flows involving shock-turbulence interaction and multi-material mixing, that were to be validated with the DNS databases generated during the program. The numerical codes developed are designed for massively-parallel computer architectures, ensuring good scaling performance. Their algorithms were validated by means of a sequence of benchmark problems.

The original multi-stage plan for this five-year project included the following milestones: 1) refinement of numerical algorithms for application to the shock-turbulence interaction problem and multi-material mixing (years 1-2); 2) direct numerical simulations (DNS) of canonical shock-turbulence interaction (years 2-3), targeted at improving our understanding of the physics behind the combined two phenomena and also at guiding the development of SGS models; 3) large-eddy simulations (LES) of shock-turbulence interaction (years 3-5), improving SGS models based on the DNS obtained in the previous phase; 4) DNS of planar/spherical RM multi-material mixing (years 3-5), also with the two-fold objective of gaining insight into the relevant physics of this instability and aiding in devising new modeling strategies for multi-material mixing; 5) LES of planar/spherical RM mixing (years 4-5), integrating the improved SGS and multi-material models developed in stages 3 and 5.

This final report is outlined as follows. Section 2 shows an assessment of numerical algorithms that are best suited for the numerical simulation of compressible flows involving turbulence and shock phenomena. Sections 3 and 4 deal with the canonical shock-turbulence interaction problem, from the DNS and LES perspectives, respectively. Section 5 considers the shock-turbulence interaction in spherical geometry, in particular, the interaction of a converging shock with isotropic turbulence as well as the problem of the blast wave. Section 6 describes the study of shock-accelerated mixing through planar and spherical Richtmyer-Meshkov mixing as well as the shock-curtain interaction problem In section 7 we acknowledge the different interactions between Stanford and other institutions participating in this SciDAC project, as well as several external collaborations made possible through it. Section 8 presents a list of publications and presentations that have been generated during the course of this SciDAC project. Finally, section 9 concludes this report with the list of personnel at Stanford University funded by this SciDAC project.

2 Collaborative assessment of numerical algorithms

The main computational challenge of predicting compressible turbulence in general, and interactions between shock waves and turbulent flows in particular, arises from the contradictory properties of numerical methods designed to treat shocks and turbulence. Shock waves are extremely thin regions of widths on the order of a few mean free paths; in the context of the present work, they are considered to be sharp discontinuities, *i.e.*, no attempt is made to resolve the physical shock structure. In order to represent shock waves in an accurate and stable fashion on a computational grid,

most numerical schemes rely strongly on numerical dissipation, which results in smearing the shock over a few grid points. Such techniques are termed *shock capturing*, as opposed to *shock tracking* or *shock fitting*, in which the shock position, shape and velocity are explicitly determined. The major drawback of using shock-capturing schemes in smooth turbulent regions is that the numerical dissipation invariably overwhelms the physical dissipation, which is precisely what numerical methods for turbulence simulations seek to avoid.

As illustrated by the broad range of algorithms in the literature, a number of different strategies have been used to overcome the difficulties of simultaneously treating shocks and turbulence. Certain methods employ purely shock-capturing finite difference approximations, *e.g.*, based on the weighted essentially non-oscillatory (WENO) schemes of Jiang and Shu (46), possibly with improved wavenumber properties (35; 58). Other methods use characteristic-based filters in conjunction with artificial compression and wavelets as flow sensors to control the numerical dissipation (73; 66). A compact scheme may be employed with adaptive Padé-type filters to stabilize the solution near shocks (39; 71). Another avenue is the hybrid approach, in which a shock detector restricts the use of shock capturing to regions near shocks in order to contain the dissipation in smooth regions (27; 60). Yet another approach consists of regularizing the governing equations by introducing numerical dissipation, *e.g.*, artificial diffusivity (32; 17; 38; 57) or hyper-diffusivity (45), and of solving the resulting system with high-order accurate methods. An alternative philosophy is to use shock fitting with an upwind scheme for problems with a single well-defined shock (77).

Analyzing the aforementioned methods theoretically is a challenging task due to their complexity; such methods are typically verified using different test problems and validated against experiments. However, it is difficult to establish a hierarchy based on the published work or even determine which method is the most appropriate for a given compressible turbulence problem because of the lack of comparisons between such schemes. At the present time, comparisons are restricted to a narrow class of methods and problems, *e.g.*, shock-capturing schemes for shock-dominated flows (54; 41); artificial diffusivity methods for shocks (32; 38; 47) or purely broadband problems (33; 17); and monotone integrated LES (42), subgrid-scale modeling for LES (49) and the evaluation of shock-capturing schemes in LES (40) for compressible turbulence.

The objective of the present study is to provide an evaluation of a suite of numerical methods that can and have been used to simulate problems in which shocks and turbulence are both present and interact dynamically. The key aspect of this work is the comprehensive range of methods *and* suite of relevant test problems that are considered to best evaluate the strengths and weaknesses of the current algorithms. Several high-resolution algorithms (WENO, hybrid WENO/central difference, artificial diffusivity, adaptive characteristic-based filter and shock fitting) are considered. Problems with purely smooth and broadband features (Taylor-Green vortex) and well-defined discontinuities (Shu-Osher problem, shock-vorticity/entropy wave interaction, Noh problem) are chosen, along with, more importantly, a combination thereof (compressible isotropic turbulence with eddy shocklets); the latter problem turns out to be surprisingly discriminating. Under-resolved results are presented to illustrate the effects of numerical dissipation on a fixed (coarse) grid; the assessment of the numerical methods considered in the present work may differ when considering the fully resolved case.

2.1 Numerical methods

The compressible Navier-Stokes equations for a calorically perfect gas are solved in this work. The first key aspect of the present work is the comprehensive nature of the numerical methods

Code	Color	Line style
Reference	black	varying
Stan	red	dashed
Stan-I	magenta	dashed (thin)
Hybrid	blue	solid
WENO	cyan	solid (thin)
ADPDIS3D	green	dashed-dotted
Shock Fit	black	dotted

Table 1: Color and line legend for the plots.

evaluated. Six high-resolution and high-order accurate methods based on different approaches to computing shock waves and turbulence are considered. Though third-order accuracy in space is typically considered high-order accurate in the literature, the present schemes are at least fifth- and up to tenth-order accurate in smooth regions. All problems are solved on uniform Cartesian grids.

Given the number of methods (and thus the number of lines in each plot), a consistent color and line scheme is used, as listed in Table 1.

The *Stan* and *Stan-I* methods are of the *artificial diffusivity* type, where the equations are regularized through addition of artifical fluid properties. One of the key findings of the present collaborative work is that the artificial bulk viscosity proposed by Cook (17) causes excessive damping of dilatational and thermodynamic fluctuations in compressible turbulence This finding prompted Mani et al. (57) to define the artificial bulk viscosity in terms of the dilatation (rather than the strain-rate tensor), to prevent excessive damping of the dilatational motions. The key improvement stems from the realization that dilatation and the magnitude of the strain-rate tensor are similar at a shock, but that the former is orders of magnitude smaller in turbulence. In order to illustrate the recent progress on artificial diffusivity methods, results from two methods using different models for the artificial bulk diffusivity but with the same underlying numerics are used in the present study:

1. *Stan*: the original model of Cook (17).

2. *Stan-I*: the improved model of Bhagatwala and Lele (29), which is based on the work of Mani et al. (57).

The *Hybrid* code (51) is based on the principle that turbulence and shock waves are fundamentally different phenomena and should thus be treated differently. Hence, to distinguish shock waves from smooth turbulent regions, the *Hybrid* method relies on a shock sensor based on vorticity and dilatation. In smooth regions, a sixth-order accurate central differencing scheme is applied in split (or 'skew-symmetric') form for improved nonlinear stability (37). In discontinuous regions, a fifth-order accurate WENO scheme is used. The hybrid nature of the code creates internal interfaces between the central and WENO regions, the stability of which was analyzed in (50).

The *WENO* code consists of a seventh-order conservative finite difference WENO scheme for the interpolation.

The *ADPDIS3D* code is based on low dissipation high-order accurate filter methods in finite difference formulation (73; 66; 75; 76). Such a filter method consists of two steps: a full time step using a spatially high-order non-dissipative base scheme, followed by a post-processing filter step.

The post-processing filter step consists of the products of wavelet-based flow sensors and linear and nonlinear numerical dissipations.

Finally, the *Shock Fit* code is based on the shock-fitting method of (77), which treats the shock as a sharp entity and solves the compressible Navier-Stokes equations in conservation form in the computational domain. The shock velocity and the flow variables behind the shock are obtained using the Rankine-Hugoniot relations coupled with a characteristic compatibility equation. The location and geometry of the shock is modified according to the shock velocity and shock-fitted curvilinear grids are used. In the shock fitting approach, any scheme can be used to solve the governing equations in the computational domain. In the present calculations, a fifth-order accurate upwind finite difference scheme (77) is used to discretize the governing equations. Results are shown only for problems with initially well-defined shocks (Shu-Osher problem and shock-vorticity/entropy wave interaction), with a fixed set of coefficients.

2.2 Some key results

The second key element in the present work is the comprehensive suite of benchmark problems. Since the end applications of interest all share the common trait of simultaneously involving broadband turbulence and sharp discontinuities (shocks and contact surfaces), the test problems are chosen in an attempt to isolate one or more relevant properties and to eventually combine them. The problems are ordered in a sequence of increasing complexity (by some measure): first the shock-free but broadband three-dimensional Taylor-Green vortex; then a series of non-broadband shock problems (one-dimensional Shu-Osher problem, two dimensional shock-vorticity/entropy wave interaction), culminating in the infinite-strength three-dimensional Noh implosion; and a three-dimensional compressible isotropic turbulence problem with broadband spectra and eddy shocklets. The last problem is the only viscous problem. Two sets of results are presented: a converged solution and a solution on a coarse grid.

2.2.1 Taylor-Green vortex

From a well-resolved initial condition, the inviscid Taylor-Green vortex (69) begins stretching and producing ever smaller scales. It thus constitutes a non-regularized problem with no lower bound on the length scale and is solved with no regularization other than that provided by the numerical method. The goal of this problem is to provide a test of the stability of the methods for severely under-resolved motions, as well as a measure of the preservation of kinetic energy and the growth of enstrophy.

Figure 1 shows the temporal evolution of the mean kinetic energy, $\langle \rho u_i u_i \rangle / 2$, and enstrophy, $\langle \omega_i \omega_i \rangle / 2$, where $\boldsymbol{\omega} = \nabla \times \mathbf{u}$ is the vorticity, normalized by their initial values.

The dilatation-based shock sensor in the *Hybrid* code never activates the WENO scheme for this problem, allowing the non-dissipative central scheme to preserve the kinetic energy. The *ADPDIS3D* code is essentially non-dissipative, with only a slight decrease toward the end of the simulation. These two methods also give the most rapid growth in enstrophy. The *WENO* code is the most dissipative of all the methods for this problem; it begins adapting its stencils at $t \approx 3$, which drastically increases the numerical dissipation, thus leading to underpredictions in the kinetic energy and enstrophy. The *Stan* code lies somewhere in between the *Hybrid*/*ADPDIS3D* and *WENO* results. Note that the improved *Stan-I* results are identical to those of *Stan* for this

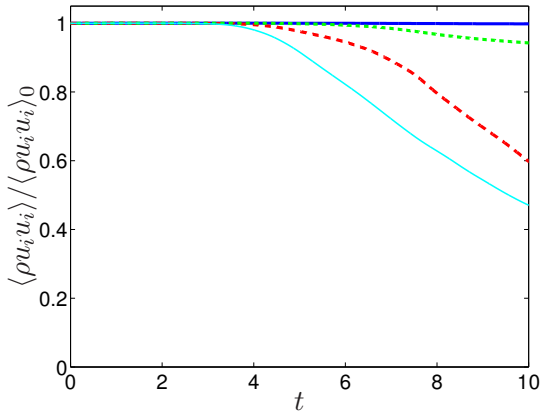

(a) Kinetic energy.

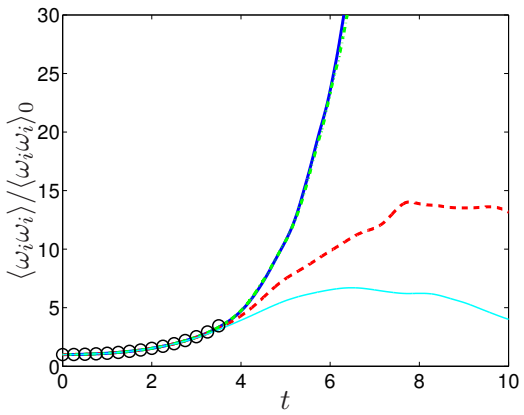

(b) Enstrophy. The semi-analytical result (30) are the black symbols.

Figure 1: Mean quantities for the Taylor-Green vortex on a 64^3 grid. The zero subscript denotes the initial value.

problem, since the solenoidal velocity field is insensitive to the bulk viscosity. On the present grid, all methods agree with the semi-analytical results for the enstrophy growth.

In order to provide a quantitative comparison of the codes, the mean kinetic energy normalized by its initial value is tabulated at $t = 5$; at this time, dissipation effects have become evident. Also, the mean enstrophy normalized by its initial value is tabulated at $t = 3.5$; this is the last time for which semi-analytical results are obtained. These two values are shown in Table 2 and exhibit a behavior similar to that plotted in Fig. 1. Such metrics provide quantitative means for other researchers to evaluate their codes against the present algorithms.

	Hybrid	*ADPDIS3D*	*Stan*	*Stan-I*	*WENO*	(30)
T-G energy $t = 5$	1.00	0.998	0.976	0.976	0.916	1.00
T-G enstrophy $t = 3.5$	3.33	3.34	3.23	3.23	3.13	3.46

Table 2: Accuracy metrics for the Taylor-Green vortex, with the semi-analytical result (30).

2.2.2 Noh problem

The Noh problem (59) consists of an infinite Mach number implosion and is relevant to inertial confinement fusion, in which strong shock waves interact with interfaces separating different fluids and with the resulting turbulence. The goal of this problem is to test the capability to handle a strong spherical shock. In particular, this problem provides an assessment of the capability to predict the post-shock density (*i.e.*, the compression by the strong shock wave), the correct shock speed, and the spherical shape on a Cartesian grid (*i.e.*, whether grid-imprinting errors are generated). The initial conditions correspond to a spherically imploding flow with uniform density and pressure. The pressure is nominally zero and leads to an infinite Mach number for the imploding flow. To prevent complex eigenvalues (which would make the problem ill-posed), a lower bound on the pressure is imposed as $p_{\min} = \epsilon = 10^{-6}$. In response to the initial imploding flow, a strong

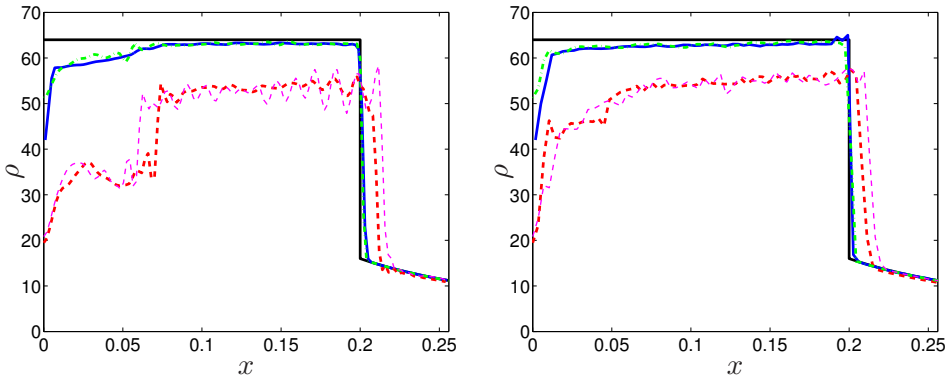

(a) Solution along the grid.

(b) Solution diagonal to the grid

Figure 2: Profiles at $t = 0.6$ for the Noh problem. The *WENO* method is not shown for clarity, but is slightly better than the *Hybrid* method; the results from the *ADPDIS3D* code are based on the divergence form of the convective terms with the addition of a tenth-order accurate linear dissipation. The reference is the analytical solution of (59).

spherical shock wave traveling outward at constant speed develops. The analytical solution for the density in three dimensions is (59)

$$\rho = \begin{cases} 64\,, & r < t/3, \\ (1 + t/r)^2\,, & r \geq t/3. \end{cases} \tag{1}$$

Shown in Figure 2 are profiles of the density along and diagonal to the grid. The *Hybrid* results are the closest to the analytical solution, with small errors in both the shock location and the spherical shape. The *Stan* and *Stan-I* codes yield larger errors in shock position and post-shock density, and larger grid imprinting errors near the origin. The original form of the bulk viscosity (*Stan*) gives a somewhat smaller error in shock position compared to the "improved" version (*Stan-I*). We note that the results from the artificial diffusivity methods for this problem in (33) are significantly better than the *Stan* results (roughly halfway between the *Stan* and *Hybrid* results on equivalent grids). The main difference between *Stan* results and those of Ref. (33) is that the former treats the convective terms on a split form; this difference is most likely to blame for the worse results by the *Stan* code. When the un-split form of the convective terms and a tenth-order linear dissipation are used for the base scheme step, a stable solution could be obtained.

In order to provide a quantitative comparison of the codes, the mean density in the spherical shell $r \in [0.15, 0.17]$ at $t = 0.6$ is listed in Table 3; this quantity provides a measure of the compression achieved downstream of the shock. The RMS of the density fluctuations in the same spherical shell is also listed in the table; this quantity provides a measure of the grid imprinting errors. The spherical shell is chosen such that errors near the center and near the shock do not affect this value. The purpose of listing these metrics is to provide quantitative means for other researchers to evaluate their codes against the present algorithms.

2.2.3 Compressible isotropic turbulence

The final test case is that of decaying compressible isotropic turbulence with eddy shocklets (52). Given a sufficiently high turbulent Mach number M_t, weak shock waves (eddy shocklets) develop

	Hybrid	*ADPDIS3D*	*Stan*	*Stan-I*	*WENO*	Exact
Noh mean density	63.2	63.3	55.1	54.9	63.3	64.0
Noh rms density	0.374	0.238	0.630	0.814	0.346	0.000

Table 3: Accuracy metrics for the Noh problem.

spontaneously from the turbulent motions. The goal of this problem is to test the ability of the methods to handle 'randomly' distributed shocklets (in the sense of the shock-locations not being known *a priori*), as well as the accuracy for broadband motions in the presence of shocks. The density and pressure fields are initially constant, with the initial parameters, $M_{t,0} = 0.6$ and $Re_{\lambda,0} = 100$. Since the initial conditions are not in acoustic equilibrium, a field of background acoustic waves develops and persists throughout the simulation. Similarly, there are initial entropy modes. We note that this particular initial condition is chosen since, for the present comparison, a problem with large acoustic and entropy modes is desirable to highlight the performance of the methods. In order to generate the reference solution, the *Hybrid*, *ADPDIS3D* and *Stan* codes were run on a sequence of grids up to 256^3. All the present methods converge on the finest grid, and agreed with each other even on a point-wise basis at the final time $t/\tau = 4$, where $\tau = \lambda_0/u_{\mathrm{rms},0}$ is the eddy turn-over time.

The temporal evolution of the mean-square velocity and vorticity, and the variance of the temperature and dilatation are plotted in Figure 3. The RMS of pressure and density exhibit a behavior similar to that of temperature and are therefore not shown. The minimally dissipative *Hybrid* code agrees well with the reference solution for all quantities. The *WENO* code underpredicts all quantities, thereby showing how dissipative it is for broadband motions. It particularly underpredicts the vorticity and dilatation, which is consistent with the fact that the WENO procedure damps the small-scale motions. The *ADPDIS3D* code agrees with the reference almost as well as the *Hybrid* code except that it is more dissipative. The original and improved artificial diffusivity methods behave similarly for the kinetic energy and the enstrophy, but the original method (*Stan*) is highly dissipative for both dilatational and temperature fluctuations; in fact, it annihilates the dilatational motions very quickly. It was this finding that spurred (57) and subsequent researchers to improve the method by making the artificial bulk viscosity sensitive to dilatational motions; the improvement in the dilatation fields of the *Stan-I* code over those of the *Stan* code is solely due to this implementation of the artificial bulk viscosity. Similarly, the predicted temperature fluctuations are significantly improved.

2.3 Conclusions

The objective of the present work is to evaluate the performance of several numerical methods on problems in which shock waves and turbulence are present and interact dynamically. Several different numerical methods (WENO, hybrid WENO/central difference, artificial diffusivity, adaptive characteristic-based filter and shock fitting) for compressible turbulence are assessed on under-resolved grids. A wide range of discriminatory problems is considered, including purely broadband (Taylor-Green vortex), shock-dominated (Shu-Osher problem, shock-vorticity/entropy wave interaction, the Noh problem), and a combination of the two (compressible isotropic turbulence). Even though qualitatively different behavior is observed in some cases, all the schemes perform well for most of the test problems. The following observations are made:

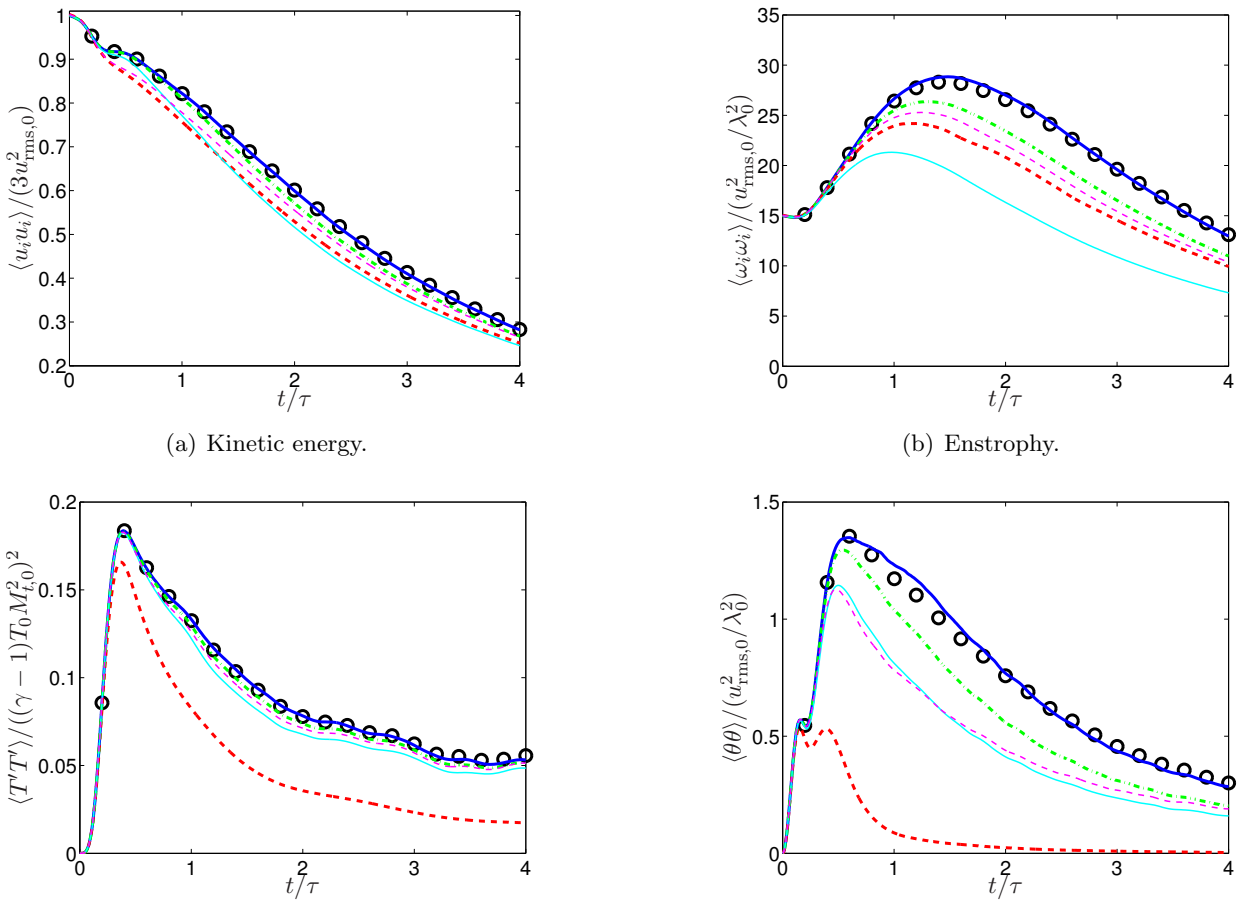

(a) Kinetic energy.

(b) Enstrophy.

(c) Temperature.

(d) Dilatation, $\theta = \partial_j u_j$.

Figure 3: Temporal evolution of the variance of different quantities for the isotropic turbulence problem on 64^3 grid. The reference is the solution on a 256^3 grid spectrally filtered to a 64^3 grid (circles).

- The WENO method provides sharp shock-capturing, but overwhelms the physical dissipation and underpredicts approximately the upper 3/4 of the resolvable wavenumbers for broadband problems.

- The artificial diffusivity method of Cook (17) performs well on the problems with either shocks *or* broadband motions, but vastly underpredicts the dilatational velocity and thermodynamic (density, pressure, temperature) fluctuations when shocks and turbulence are interspersed; in fact, even WENO yields better results for the dilatation and thermodynamic fluctuations. The reason for this behavior is that the artificial bulk viscosity is based on the strain-rate magnitude, such that its value is both large and rapidly varying in turbulent regions. Hence, this formulation leads to a large bulk viscosity, which in turn annihilates dilatational motions. This behavior is improved by re-defining the artificial bulk viscosity to be a function of the dilatation.

- The Noh problem illustrates how the use of a split ('skew-symmetric') scheme negatively affects the capturing of a strong shock: it decreases the shock compression in the artificial diffusivity method. The hybrid WENO/central difference method avoids this issue by switching to a conservative formulation in the WENO region.

- The comprehensive nature of the test problems in this study proved to be a challenge in terms of defining a shock sensor in the hybrid WENO/central difference method. The dilatation/vorticity sensor works adequately for these problems, although it does so in an unintended way for the turbulence-free problems.

- The compressible isotropic turbulence problem with eddy shocklets proved to be a challenging problem because weak shocks are interspersed with turbulence and all compressible modes (vortical, entropic, acoustic) are present.

Based on these observations, we can make the following recommendations:

- WENO and the original artificial diffusivity method of Cook (17) in their standard forms are not suitable for high-fidelity computations of compressible turbulence. If used, they must be accompanied with convincing grid refinement studies clearly showing sufficient grid resolution. While this statement is true for every method, it is particularly true for highly dissipative methods. Simply showing that spectra are decaying at the highest wavenumbers is not sufficient, since this is a built-in feature of dissipative methods.

- The modified artificial diffusivity methods that use dilatation rather than strain-rate magnitude to activate the artificial bulk viscosity are substantial improvements over the originial method of Cook (17), and make the method suitable for compressible turbulence calculations.

- The benefits of minimizing numerical dissipation (*e.g.*, by restricting the regions in which it is applied) are clear. The main challenge for the hybrid central/WENO method lies in the shock-sensor.

- The main advantage of shock fitting (over shock capturing) is that it avoids post-shock oscillations. The main challenge is that it is difficult to apply to shocks with complex and/or changing topology.

3 DNS of canonical shock-turbulence interaction

Given the historical success of studying simplified problems in furthering our physical understanding, we have focused on the canonical problem of isotropic turbulence interacting with a normal shock in a perfect gas. Figure 4 shows the essence of the problem, and the modification of the turbulence during the shock-interaction is evident. Prior to our SciDAC-funded work the largest computations in the literature had a Reynolds number of $Re_\lambda \approx 20$ (based on the Taylor-scale), a maximum turbulent Mach number of $M_t \approx 0.1$, and grid-resolutions on the order of 100^3.

Our approach was to perform direct numerical simulation (DNS) in the sense of fully resolving all scales of turbulence but numerically capturing the shock wave, which is treated as a discontinuity. The study progressed in several steps. We first computed a set of 14 cases at different combinations of (M, M_t) (M is the mean Mach number of the shock) at $Re_\lambda \approx 40$ on 1040×384^2 grids. These

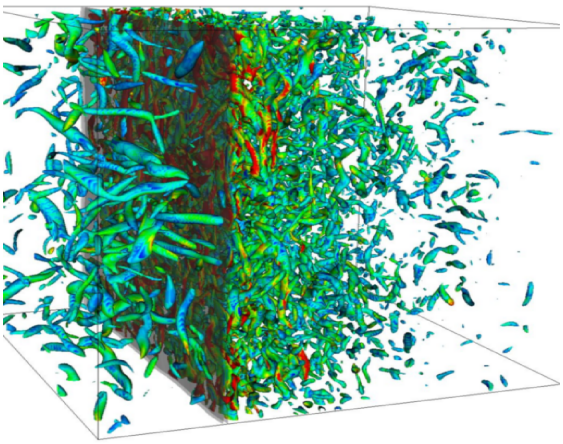

Figure 4: Snapshot of canonical shock-turbulence interaction. Turbulent eddies (colored by their rate-of-rotation) enters from the left and passes through the shock (thin dark sheet). The interaction increases the rate-of-rotation, the turbulence kinetic energy, and makes the post-shock turbulence anisotropic.

simulations showed an at first surprising result: that the characteristic size of the smallest eddies (where dissipation of kinetic energy into heat occurs) becomes markedly smaller during the shock-interaction. Prior simulations in the literature had not taken this effect into account, and hence our DNS results were the first ever to fully resolve the post-shock viscous dissipation. This, in turn, affects the post-shock evolution of the turbulence. Figures 5 and 6 show two statistical quantities far behind the shock, contrasted with the leading linear theory by Ribner (1) and the experiments by Barre *et al.* (78). The agreement/disagreement between the 3 sets of data strongly suggests both that the amplification of turbulence kinetic energy is a linear, large-scale process, but also that the shock-induced change in the turbulence structure is a nonlinear process that the theory fails to capture.

Figure 7 shows some instantaneous pathlines through the shock. The fact that the turbulence has created instantaneous "shock-holes" had been seen in prior studies, but the presence at Mach numbers higher than 1.05 was first seen in this study. Considerable time was spent on analyzing the instantaneous structure of the shock/turbulence interaction, including through visualizations such as shown in figure 8.

These simulations at $Re_\lambda \approx 40$ were run at NERSC (under the ERCAP program) and ANL (under the INCITE program) on up to 8,192 cores. The results of this study were published in (3). Since then, we have run 4 additional DNS cases at a higher Reynolds number of $Re_\lambda \approx 75$ on 2234×1024^2 grids. These cases were run on either 65,536 cores on the BG/P at ALCF or 12,288 cores on the Cray XT-4 at NERSC. The purpose of these additional cases is to elucidate the effect of Reynolds number on the shock-turbulence interaction problem, which is important due to the disparity in Re between experiments and real-world applications (generally very high Re) and computations (rather low Re due to the very high cost associated with resolving the compressed post-shock turbulence). These additional cases have been run and analyzed; the results form the basis for a paper that has been submitted to the Journal of Fluid Mechanics.

The *Hybrid* code which was used for these runs was designed specifically to minimize the numerical (and unphysical) dissipation, thereby increasing the fidelity of the results. The code

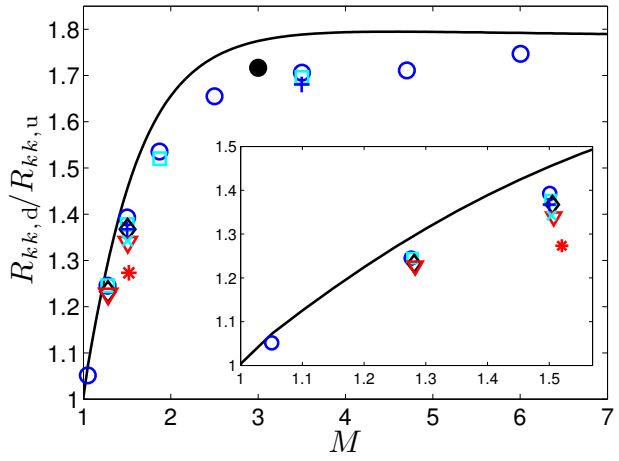

Figure 5: Amplification of the turbulence kinetic energy across the shock versus Mach number, where the post-shock R_{kk} is defined through spatial extrapolation to the mean shock position. At each Mach number, the cases are shown with different symbols in order of increasing M_t. At $Re_\lambda \approx 40$ the symbols are, in order: circle, square, diamond, and triangle. At $Re_\lambda \approx 70$ the symbols are, in order: plus, cross, and star. Compared to result from linear interaction analysis (solid, taken from Sinha *et al.* 79) and experiments by (78) using hot-wire anemometry for R_{11} combined with LDV measurements of R_{11}/R_{22} (solid circle).

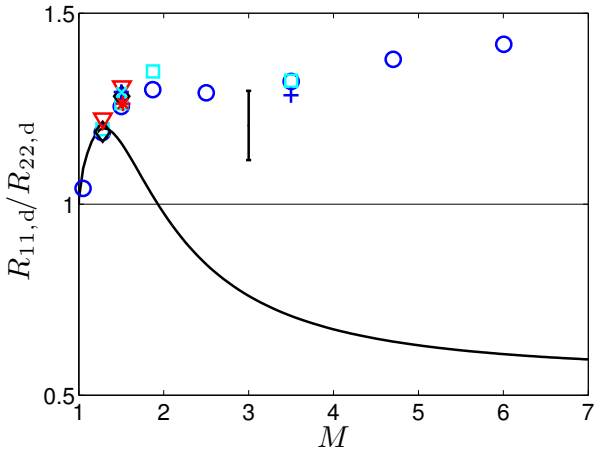

Figure 6: Mach number dependence of the post-shock turbulence anisotropy in the far-field. At each Mach number, the cases are shown with different symbols in order of increasing M_t. At $Re_\lambda \approx 40$ the symbols are, in order: circle, square, diamond, and triangle. At $Re_\lambda \approx 70$ the symbols are, in order: plus, cross, and star. Compared to result from linear interaction analysis (solid, taken from Sinha *et al.* 79) and experiments by (78) using LDV (errorbar showing the experimental rms-variation in the far-field).

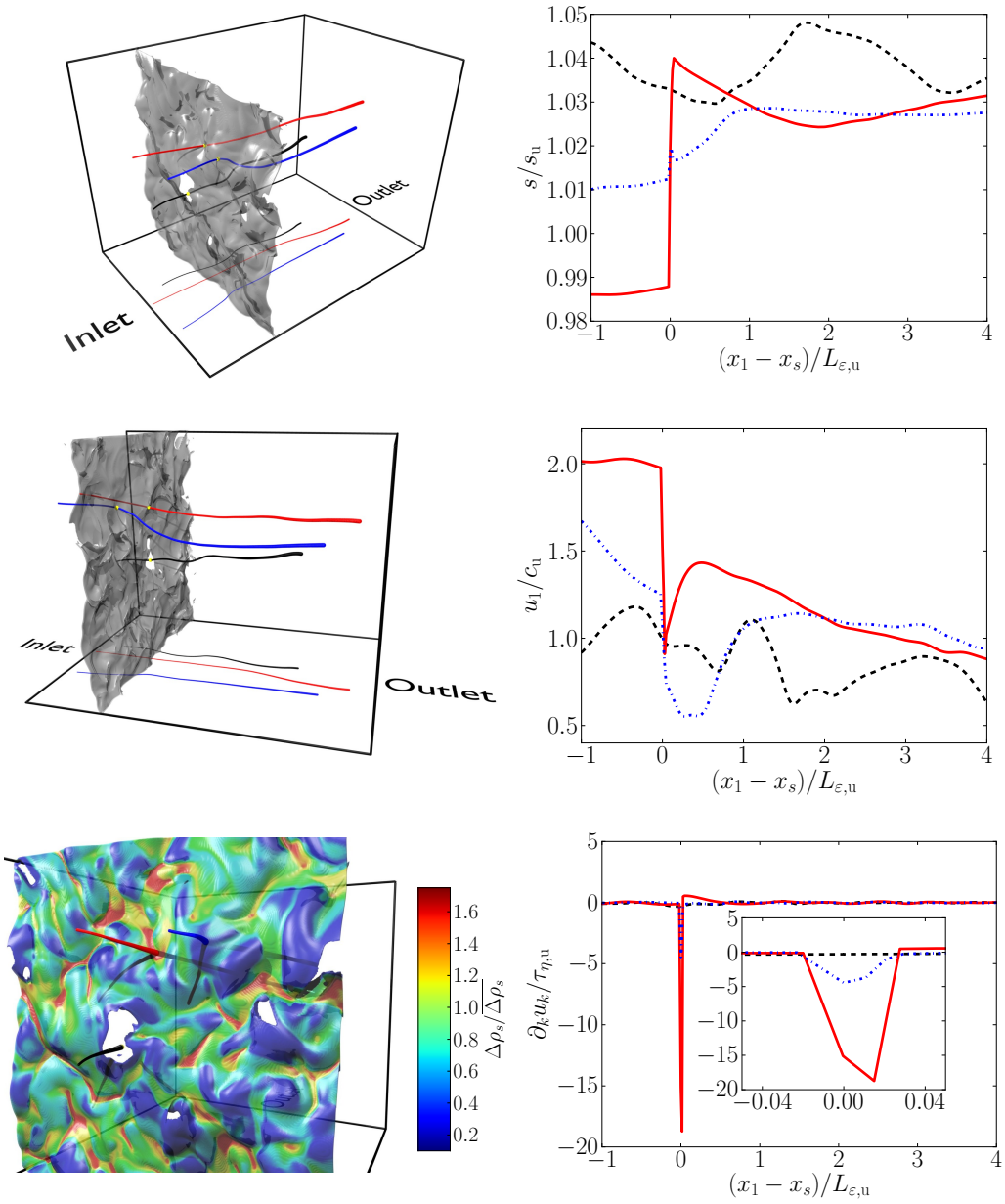

Figure 7: Instantaneous pathlines of three fluid particles at $(M, M_t) = (1.51, 0.37)$ and $Re_\lambda = 39$ that crossed the shock at the same time, in regions of very high compression (solid), relatively low compression (dash-dotted), and virtually zero compression (a "shock-hole"; dashed line). Left: 3D views (top and center) of the pathlines together with an isosurface of negative dilatation visualizing the shock (gray surface) at the time when the particles traverse it (marked by a yellow dot for each particle). The projections of the pathlines on the bottom plane of the domain are included for clarity. A zoomed view of the particle trajectories at the instant when they crossed the shock is shown on the bottom left plot, with the shock colored by the local density jump across it, normalized with the average density jump. Right: Traces of entropy, shock-normal velocity and dilatation (top to bottom) along the three pathlines, plotted as functions of the shock-normal coordinate relative to the shock position at the time the particle crossed the shock.

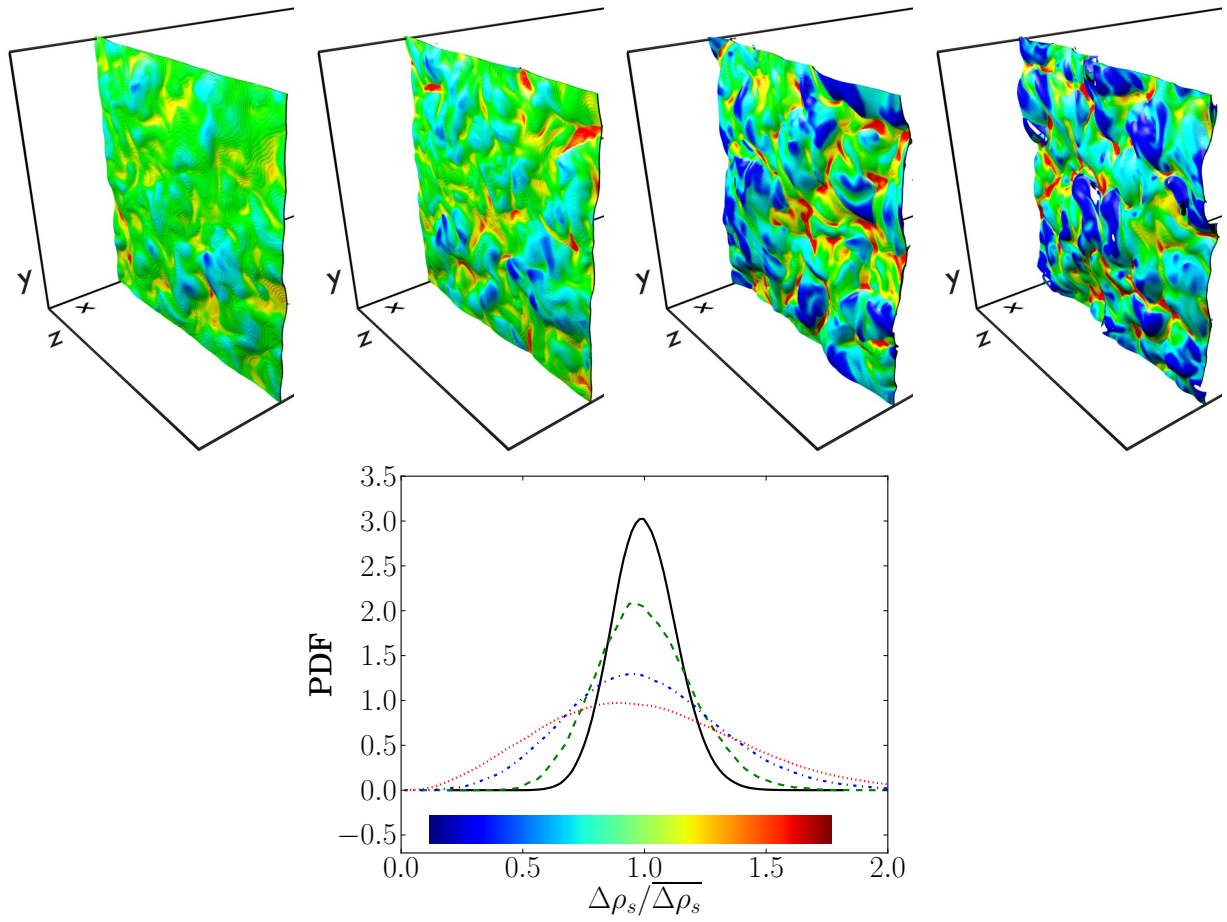

Figure 8: Instantaneous shock strength and shape for increasing M_t at fixed $M = 1.50$ and $Re_\lambda = 40$. Top: Instantaneous shock educed through isocontour of negative dilatation colored by the density jump, $\Delta\rho_s$, for $M_t = 0.16, 0.22, 0.31, 0.38$ (from left to right). Bottom: PDF of the normalized density jump for M_t of 0.16 (solid), 0.22 (dashed), 0.31 (dash-dotted), 0.38 (dotted).

scales very well due to the fully explicit spatial/temporal nature of the method and the overlapping computation/communication. On the BG/P, the weak scaling efficiency is 98% when going from 4 to 65,536 cores, and the strong scaling efficiency is above 85% when going from 256 to 65,536 cores (where each processor has only $8 \times 16^2 = 2048$ points).

Finally, we note that we have shared the computed DNS data sets with other researchers who are using them to devise improved engineering models (within the DOE PSAAP program and at the Indian Institute of Technology at Madras), improved large-eddy simulation models (both within our SciDAC project and at TU Munich, Germany), and to elucidate the interaction-physics (at Texas A&M University).

4 LES of canonical shock-turbulence interaction

The DNS databases of the canonical shock-turbulence interaction problem obtained as a result of the work described in section 3 and reported in (4) are used to compare the performance of several SGS models for large-eddy simulations (LES) of such flow type, focusing on the region immediately downstream of the shock, which poses most of the modeling challenges (5).

4.1 Mathematical formulation and numerical method

We consider the following LES formulation for conservation of mass, momentum and total energy:

$$\partial_t \overline{\rho} + \partial_j(\overline{\rho}\widetilde{u}_j) = 0 \tag{2}$$

$$\partial_t(\overline{\rho}\widetilde{u}_i) + \partial_j(\overline{\rho}\widetilde{u}_i\widetilde{u}_j) = -\partial_j\overline{p} + \partial_j\check{d}_{ij} - \partial_j\tau^S_{ij} \tag{3}$$

$$\partial_t(\overline{\rho}\widetilde{e}_T) + \partial_j(\overline{\rho}\widetilde{e}_T\widetilde{u}_j) = -\partial_j(\overline{p}\widetilde{u}_j) + \partial_j(\check{d}_{ij}\widetilde{u}_i) - \partial_j\check{q}_j - c_p\partial_j q^S_j, \tag{4}$$

where ρ is the density, t the time, u_i the velocity component in the x_i-direction, p the thermodynamic pressure, T the temperature and e_T the total energy. For a flow variable f, $\overline{f}$ denotes the LES filtering operation, $\widetilde{f} = \overline{\rho f}/\overline{\rho}$ is the Favre (density-averaged) quantity, and $\check{f}$ refers to the formal expression of f with all constituent variables replaced with their Favre-filtered counterparts: $\check{d}_{ij} \equiv d_{ij}(\widetilde{T}, \widetilde{\mathbf{u}}) \equiv \mu(\widetilde{T})\left[(\partial_j\widetilde{u}_i + \partial_j\widetilde{u}_j) - (2/3)\partial_k\widetilde{u}_k\delta_{ij}\right]$, and $\check{q}_j \equiv q_j(\widetilde{T}) \equiv \kappa(\widetilde{T})\partial\widetilde{T}/\partial x_j$. The shear viscosity is given by a power law of temperature, $\mu(T) = \mu_0(T/T_0)^{3/4}$ and the thermal conductivity, κ, is related to the viscosity through a constant Prandtl number, Pr: $\kappa(T) = c_p\mu(T)/Pr$, where c_p is the heat capacity at constant pressure. The bulk viscosity has been considered nil. The differential equations are completed with the equation of state for an ideal gas: $\overline{p} = R\,\overline{\rho}\widetilde{T}$, where R is the specific gas constant. The modeling terms considered in this study are the SGS stress tensor, τ^S_{ij} (both its trace and deviatoric part), the SGS heat flux, q^S_j, and the SGS pressure-velocity correlation term, which, for the total energy equation, can be reformulated in terms of the SGS heat flux as $\overline{pu_j} - \overline{p}\widetilde{u}_j = Rq^S_j$, by using the equation of state, as already accounted for in Equation (4) through the c_p coefficient pre-multiplying the divergence of SGS heat flux. Other modeling terms (see (5)), such as the SGS turbulent diffusion and the SGS viscous diffusion, are neglected.

The computational domain is a rectangular box of dimensions $3\pi \times (2\pi)^2$ in the streamwise (x) and transverse (y, z) directions. The equations are numerically solved using a finite-difference methodology. A solution-adaptive, hybrid approach is utilized to numerically approximate the inviscid fluxes. It combines a seventh-order accurate weighted essentially non-oscillatory (WENO) scheme near shock waves with a sixth-order accurate central-difference scheme, on the split form

of (6), elsewhere. Shock waves are identified by means of the sensor $s = -\partial_j u_j / (|\partial_j u_j| + \langle \omega_j \omega_j \rangle_{YZ}^{1/2})$, where $\langle \cdot \rangle_{YZ}$ is the instantaneous average on transverse planes and ω_i is the vorticity. WENO is only applied in the streamwise direction, for grid points where $s > 0.6$. The same sixth-order central difference scheme is applied to the viscous terms everywhere. Integration in time is accomplished through a fourth-order Runge-Kutta method.

The inflow turbulence is generated by means of an independent DNS of isotropic decaying turbulence with an initial von Kármán spectrum that peaks at a wavenumber $k = k_0 = 6$. To ensure that the turbulence is fully developed, the DNS is allowed to decay for approximately three eddy-turnover times. After the decay, the Taylor microscale Reynolds number is $Re_\lambda \approx 75$. The LES resolutions chosen for this study ensure that the cutoff wavenumber lies within the inertial range of the DNS. This inflow turbulence is then top-hat filtered to the LES resolution and advected with a uniform streamwise velocity at the inlet of the LES domain, resulting in a mean Mach number of the incoming flow of $M = 1.5$. A second case with $M = 3.5$ will be also considered. The turbulent Mach number (defined as the ratio between the turbulent kinetic energy and the sound speed) at the inlet in both cases is $M_t = 0.16$. The shock location is stationary in time on average, by imposing a mean back pressure at the outlet (4). A sponge layer extends $2\pi/3$ upstream from the outlet, to prevent propagation of spurious reflections of acoustic waves at the outflow boundary back into the computational domain, since the flow downstream of the shock is subsonic. Periodic boundary conditions apply in the transverse directions.

4.2 Subgrid-scale models implemented

Two classes of SGS models are implemented: mixed eddy-diffusivity and structure-based models. The former assumes that the effect of turbulent subgrid scales can be represented by a gradient diffusion law through an appropriate eddy diffusivity, possibly complemented with an additional term (e.g., based on scale invariance), whereas the latter assumes the SGS motion to be produced by an ensemble of coherent structures from which the closure terms are derived.

4.2.1 Mixed eddy-diffusivity models

For a general SGS closure term $\zeta = \overline{\rho}(\widetilde{u_i \eta} - \widetilde{u}_i \widetilde{\eta})$, where $\eta(\mathbf{x}, t)$ is a flow variable that will be later particularized for each (scalar, vectorial or tensorial) quantity ζ to be modeled (see Table 4), a mixed eddy-diffusivity model assumes the form $\zeta^{\text{model}} = \mathcal{MT} + \mathcal{ED}$, where $\mathcal{ED}$ is an eddy-diffusivity term and $\mathcal{MT}$ is the mixed term.

The eddy-diffusivity term is expressed as $\mathcal{ED} = \overline{\rho} \nu_e(u_i) \mathcal{G}(\widetilde{\eta})$, where $\nu_e(\widetilde{u}_i) = c_e \vartheta(\widetilde{u}_i)$ is the eddy diffusivity that depends on the resolved velocity field through a function $\vartheta(\widetilde{u}_i)$, and incorporates the model coefficient, c_e. The function $\mathcal{G}(\widetilde{\eta})$ mimics the corresponding physical diffusion law (typically of the form of a turbulent gradient) for the modeled quantity (see Table 4). Two different forms of eddy diffusivity are considered in this study: Smagorinsky's version ((7)) is based on the assumption of a Newtonian-viscous-like SGS stress tensor, dimensional analysis and a simplified balance of turbulent kinetic energy between production and dissipation that neglects convective and diffusive terms, resulting in $\vartheta^{\text{Smag}} = \Delta^2 |\widetilde{S}|$, where $|\widetilde{S}| \equiv (2 \widetilde{S}_{ij} \widetilde{S}_{ij})^{1/2}$, $\Delta = (\Delta_1 \Delta_2 \Delta_3)^{1/3}$ and Δ_i is the local grid spacing in the x_i-direction; Vreman's version ((8)) is based on the second invariant, II_β, of the tensor $\beta_{ij} = \Delta_k^2 \partial_i \widetilde{u}_k \partial_j \widetilde{u}_k$, whose collection of all local flow types with n zero velocity derivatives ($n \in [0, 9]$) equals that of the theoretical SGS dissipation, $-\tau_{ij}^S \widetilde{S}_{ij}$. By adding

SGS quantity	ζ	η	$\mathcal{G}$	c_e
Kinetic energy, $K^S = \frac{1}{2}\tau_{ii}^S$	τ_{ii}^S	u_i	$2\lvert\widetilde{S}\rvert$	C_I
Deviatoric stress tensor, $\tau_{ij}^S - \frac{1}{3}\tau_{kk}^S\delta_{ij}$	τ_{ij}^S	u_j	$-2\widetilde{S}_{ij}$	C
Heat flux	q_i^S	T	$-\partial\widetilde{T}/\partial x_i$	C/Pr_t

Table 4: Modeled SGS quantities; associated η variable; eddy-diffusivity functional dependence, $\mathcal{G}$; coefficients, c_e.

a realizability condition and imposing the correct behavior at the wall ($\nu_e = 0$), it is obtained $\vartheta_e^{\text{Vrem}} = [II_\beta/(\partial_j\widetilde{u}_i\partial_j\widetilde{u}_i)]^{1/3}$.

Three alternative mixed terms, $\mathcal{MT}$, are considered. The first option assumes a nil term, $\mathcal{MT}_1 \equiv 0$, obtaining a purely eddy-diffusivity model. In the other two alternatives, the closure term ζ is expanded in Galilean-invariant components, one of which, the Leonard term $\mathcal{L} = \overline{\rho}(\widetilde{\widetilde{u}_i\widetilde{\eta}} - \widetilde{\widetilde{u}_i}\widetilde{\widetilde{\eta}})$, is modeled by the mixed term. The *gradient mixed-term* approach uses a Taylor series expansion of the Leonard term, assuming that the Favre-filter can be approximated by either a Gaussian or a top-hat filter, resulting in the form $\mathcal{MT}_2 = \overline{\rho}\Delta_k^2\widetilde{u}_{i,k}\eta_{,k}/12$. The *similarity mixed-term* approach approximates the unknown Favre-filter by an assumed numerical low-pass filter, $\mathcal{F}$, computing the Leonard term directly as $\mathcal{MT}_3 = \overline{\rho}(\widetilde{\widetilde{u}_i\widetilde{\eta}} - \widetilde{\widetilde{u}_i}\widetilde{\widetilde{\eta}}) \approx \overline{\rho}[\mathcal{F}(\widetilde{u}_i\widetilde{\eta}) - \mathcal{F}(\widetilde{u}_i)\mathcal{F}(\widetilde{\eta})]$.

The model coefficient, c_e, is dynamically calculated following Germano's procedure (9), by means of a test-filter, denoted by $\widehat{(\cdot)}$, which is applied on the resolved flow variables. It is assumed that the same model form and model coefficient apply at the resolved and test-filtered scales and that the variation of c_e within the test-filter width is negligible compared to that of $\chi \equiv \overline{\rho}\vartheta(\widetilde{u}_i)\mathcal{G}(\eta)$, obtaining

$$\Lambda \equiv \zeta^L - (\mathcal{MT}^T - \widehat{\mathcal{MT}}) = c_e(\chi^T - \widehat{\chi}) \equiv c_e\Upsilon, \tag{5}$$

where $\zeta^L \equiv \widehat{\overline{\rho}\widetilde{u}_i\widetilde{\eta}} - \widehat{\overline{\rho}\widetilde{u}_i}\widehat{\overline{\rho}\widetilde{\eta}}/\widehat{\overline{\rho}}$, $\mathcal{MT}^T \equiv \widehat{\overline{\rho}}(\widehat{\widetilde{u}_i\widetilde{\eta}} - \widehat{\widetilde{u}_i}\widehat{\widetilde{\eta}})$, $\chi^T \equiv \widehat{\overline{\rho}}\vartheta(\widehat{\widetilde{u}_i})\mathcal{G}(\widehat{\widetilde{\eta}})$. Then, c_e can be determined by minimizing (in a least-squares sense that follows (10)) the total error in a given domain Ω, $E \equiv \int_\Omega(\Lambda - c_e\Upsilon)^2 W\mathrm{d}\Omega$: $\delta E/\delta c_e = 0 \Rightarrow c_e = I_{\Lambda\Upsilon}/I_{\Upsilon\Upsilon}$, where $I_{AB} = \int_\Omega ABW_e\mathrm{d}\Omega$ and W is a weighting function defined in Ω, which can be spatial and/or temporal. Different choices of Ω and W_e have been proposed in the literature. When W is the Dirac-delta function, c_e results in a local quantity, which has been found to be highly fluctuating in space, thus violating one of the assumptions on which the Germano procedure is based. A remedy is to use directions of homogeneity, when available, that translate the integrals $I_{\Lambda\Upsilon}$ and $I_{\Upsilon\Upsilon}$ into spatial averages (either in volume, planes or lines). Alternatively, a Lagrangian averaging procedure (proposed for incompressible flows by (11)) uses a particular combination of temporal domain Ω and a weighting function $W(t)$ following fluid particle trajectories, which makes it applicable to any flow type, regardless of inhomogeneity.

In the canonical shock-turbulence interaction flow, transverse planes parallel to the nominal shock can be approximately considered homogeneous. As the intensity of the incoming turbulence increases, the shock becomes more corrugated or even broken, and the approximation of homogeneity in transverse planes may lead to incorrect results in the computation of the model coefficients near the shock, making the use of Lagrangian averaging advantageous. In this study, the two averaging strategies (on transverse planes and along Lagrangian trajectories) will be considered. In the Lagrangian averaging, the initialization of the model coefficients (C_I, C and C/Pr_t)

is done with the values obtained from an independent LES of decaying isotropic turbulence with a pure eddy-diffusivity model and both Smagorinsky and Vreman eddy diffusivities, resulting in $(0.0768, 0.0256, 0.0256)$ and $(0.074, 0.0164, 0.0234)$ for each type of eddy diffusivity, respectively.

In this study, the discrete test-filter $\widehat{f}_i = \sum_{k=-N}^{N} a_k f_{i+k}$ used in the dynamic procedure has coefficients $a_k = (1/4, 1/2, 1/4)$, $N = 1$ and width $\sqrt{6}$, whereas the unknown Favre-filter in the similarity mixed term is approximated by a discrete filter with coefficients $(1/8, 3/4, 1/8)$ and width $\sqrt{3}$ (based on the second-order moment of the filter kernel).

4.2.2 Stretched-vortex model

The stretched-vortex model, originally developed for incompressible flows in (12) and extended to compressible flows in (13), is a structural model which assumes the subgrid motion in each cell to be produced by a superposition of nearly axisymmetric vortices, whose ensemble dynamics can be characterized by a vortex aligned with the unit vector e^v, modeled through a delta-function probability density function (pdf). The SGS stresses are then defined as $\tau_{ij}^S = \overline{\rho} K(\delta_{ij} - e_i^v e_j^v)$, where $\overline{\rho} K = \overline{\rho} \int_{k_c}^{\infty} E(k) \mathrm{d}k = \tau_{kk}^S/2$ is the SGS turbulent kinetic energy ($k_c = \pi/\Delta$ is the cutoff wavenumber), which is estimated assuming the form of the energy spectrum proposed by (14). The SGS heat flux is modeled by means of the SGS scalar flux model (15) as $q_i^S = (\Delta/2)\sqrt{K}(\delta_{ij} - e_i^v e_j^v)\partial\widetilde{T}/\partial x_j$.

A vortex orientation model has to be specified for $\mathbf{e}^v$ to be defined. Two different models are considered in this study: the first, denoted V1, assumes the vortex to be aligned with the most extensional eigenvector, $\widetilde{\mathbf{e}}_3$, of the resolved strain-rate tensor, $\widetilde{S}_{ij}$, associated with the eigenvalue λ_3; the second, V2, uses a local pdf of the form $P(\mathbf{e}^v) = \theta\delta(\mathbf{e}^v|\widetilde{\mathbf{e}}_3) + (1-\theta)\delta(\mathbf{e}^v|\widetilde{\mathbf{e}}_\omega)$, where $\widetilde{\mathbf{e}}_\omega$ is the unit vector of the resolved vorticity (ω_i), $\delta(\mathbf{m}|\mathbf{n})$ is the delta-function probability density that $\mathbf{m}$ is aligned with $\mathbf{n}$, and θ is the fraction of SGS vortices aligned with $\widetilde{\mathbf{e}}_3$, given by the ansatz $\theta = \lambda_3/(\lambda_3 + \sqrt{\widetilde{\omega}_i\widetilde{\omega}_i})$.

4.3 Conditional application of SGS models in a hybrid methodology

As discussed in Section 4.1, a hybrid approach that applies a WENO scheme in regions near shock waves and a central-difference scheme elsewhere is used. To capture shock waves, WENO schemes add excessive numerical dissipation, damping the turbulence in those regions, which affects the post-shock turbulence (see (16)). Further application of an SGS model in WENO regions can result in an overly dissipative combination, which can be avoided by conditioning the application of the SGS model to flow regions where WENO is not active. The same WENO sensor is used by the SGS model to set the modeled SGS terms to zero. This is done prior to the calculation of the divergence of those SGS terms, as they appear in the equations of motion, ensuring conservation of momentum and total energy. Results of LES with and without this conditional SGS application in use will be compared in Section 4.4. Note that this technique is independent of the SGS model in use.

When Lagrangian averaging is used for eddy-diffusivity models, regions where the model is not active simply transport the model coefficients from the previous point of the fluid particle trajectory, and thus, across the shock wave region. A more elaborate approach could incorporate theoretical elements of linear interaction analysis (LIA) or rapid distortion theory (RDT) to modify the model coefficients across the shock wave, instead of transporting them from the upstream side to the downstream (which assumes the same level of turbulence on both sides). We use the latter

ID	Class	Mixed term	Eddy-diffusivity/ orientation model	Averaging	Line style
MNSP	Mixed	None	Smagorinsky	Transverse planes	Red solid
MGSP	Mixed	Gradient	Smagorinsky	Transverse planes	Red dashed
MSSP	Mixed	Similarity	Smagorinsky	Transverse planes	Red dotted
MNSL	Mixed	None	Smagorinsky	Lagrangian	Green solid
MGSL	Mixed	Gradient	Smagorinsky	Lagrangian	Green dotted
MSSL	Mixed	Similarity	Smagorinsky	Lagrangian	Green dashed
MNVP	Mixed	None	Vreman	Transverse planes	Brown solid
MGVP	Mixed	Gradient	Vreman	Transverse planes	Brown dashed
MSVP	Mixed	Similarity	Vreman	Transverse planes	Brown dotted
MNVL	Mixed	None	Vreman	Lagrangian	Blue solid
MGVL	Mixed	Gradient	Vreman	Lagrangian	Blue dashed
MSVL	Mixed	Similarity	Vreman	Lagrangian	Blue dotted
SPM	Stretched-vortex	N/A	Extensional (V1)	Transverse circle	Cyan solid
SPL	Stretched-vortex	N/A	Local pdf (V2)	Transverse circle	Cyan dashed

Table 5: Implemented models.

approach for its simplicity. Note also that the values of the coefficients will adjust dynamically to the actual new levels of turbulence found downstream.

4.4 Results

LES results are compared with filtered DNS data through streamwise profiles obtained from averaged statistics in time and across transverse planes for two different mean Mach numbers of the incoming flow ($M = 1.5$, 3.5). LES are performed on an isotropic grid G1 with 98×64^2 points, for which the LES cut-off is still separated from the large scales. For the $M = 1.5$ case we also present results for a second grid G2 which doubles the resolution in the streamwise direction (i.e., 196×64^2 points). The DNS used for comparison was performed on a grid with 2234×1024^2 points, stretched in the streamwise direction to allow a three-fold increase of the resolution at and behind the shock and later filtered to each LES resolution.

Mean flow quantities obtained from the LES show good agreement with the filtered DNS results and are not presented. We focus on turbulence-related quantities, namely the streamwise and transverse Reynolds stresses normalized with their values upstream of the shock, R_{xx}/R^u_{xx} and R_{yy}/R^u_{yy}, their anisotropy, the turbulent kinetic energy, TKE, and the SGS dissipation, $-\tau^S_{ij}\widetilde{S}_{ij}$. Figures 9, 10 and 12 contain plots of these quantities, for the implemented models specified in Table 5. Filtered DNS and no-model LES are included for comparison. We plot the subdomain $x - x_s \in [-1.25, 5]$, which excludes the sponge region near the outlet and part of the upstream region farther from the shock.

For $M = 1.5$ and grid G1, the shape of the profile of normalized streamwise Reynolds stress, R_{xx}/R^u_{xx} (Figure 9a), is well captured by most models, although the amplification level across the shock is overestimated by all models. Mixed models with Vreman's eddy-diffusivity present the best agreement with filtered DNS data and lead to rates of change upstream and downstream of

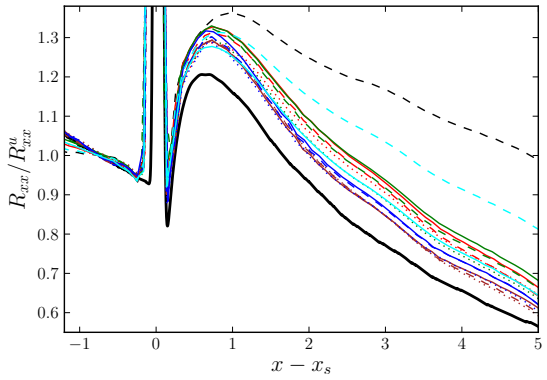

(a) Normalized streamwise Reynolds stress

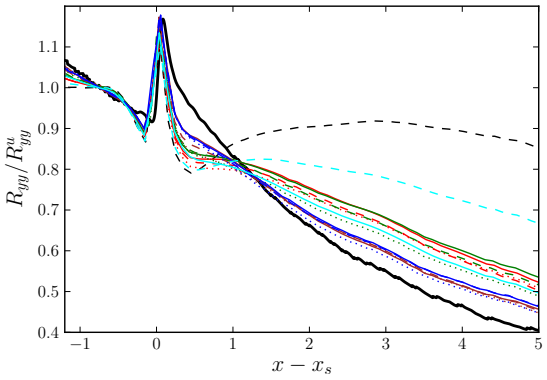

(b) Normalized transverse Reynolds stress

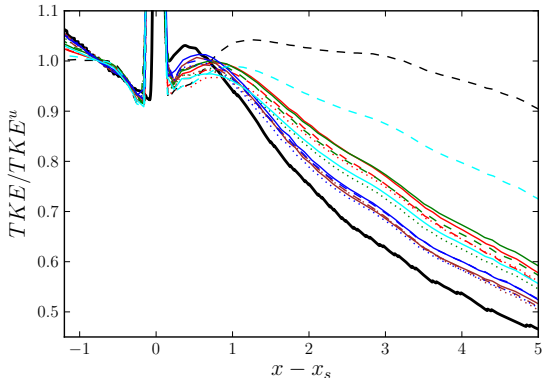

(c) Normalized turbulent kinetic energy

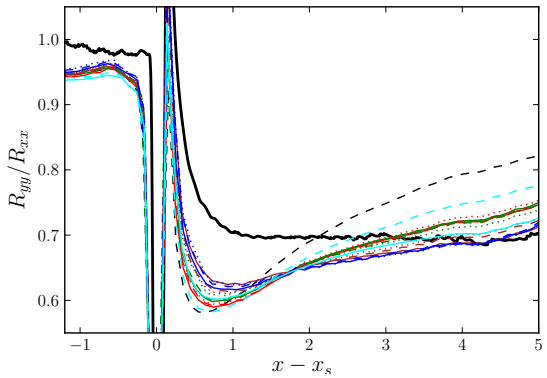

(d) Reynolds stress anisotropy

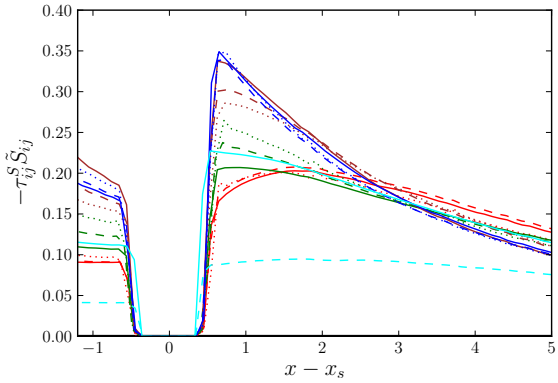

(e) Subgrid-scale dissipation

Figure 9: LES results for $M = 1.5$ and grid G1. Filtered DNS, solid black; no-model LES, dashed black. See Table 5 for SGS-LES line styles.

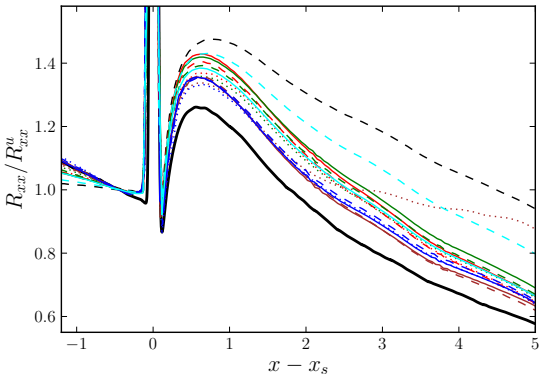

(a) Normalized streamwise Reynolds stress

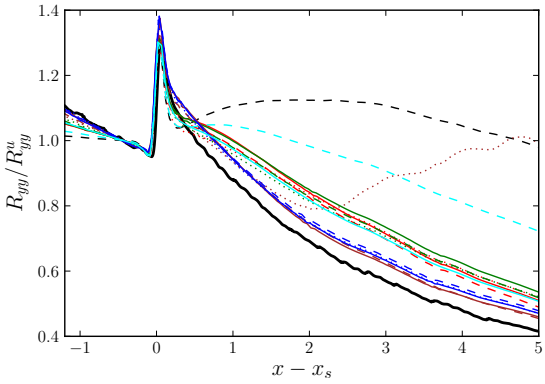

(b) Normalized transverse Reynolds stress

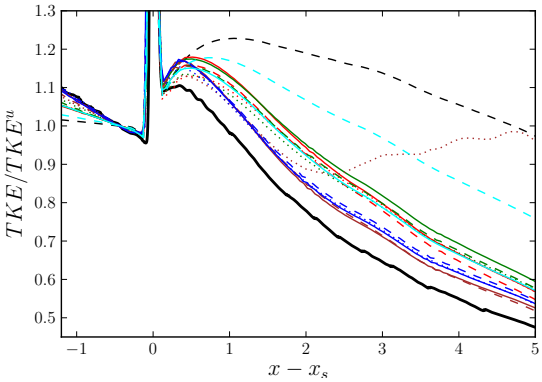

(c) Normalized turbulent kinetic energy

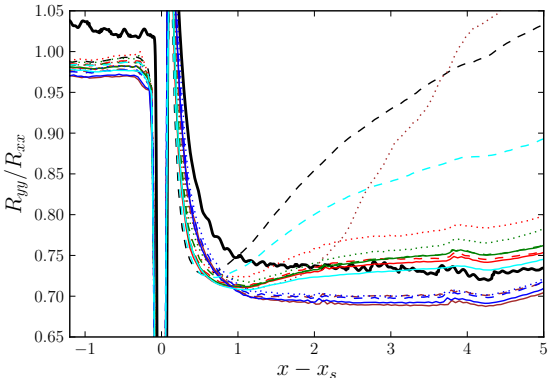

(d) Reynolds stress anisotropy

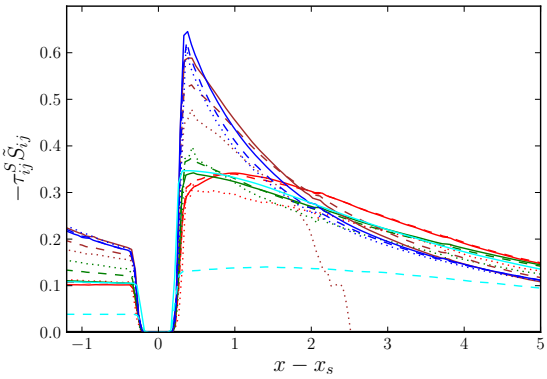

(e) Subgrid-scale dissipation

Figure 10: LES results for $M = 1.5$ and grid G2. Filtered DNS, solid black; no-model LES, dashed black. See Table 5 for SGS-LES line styles.

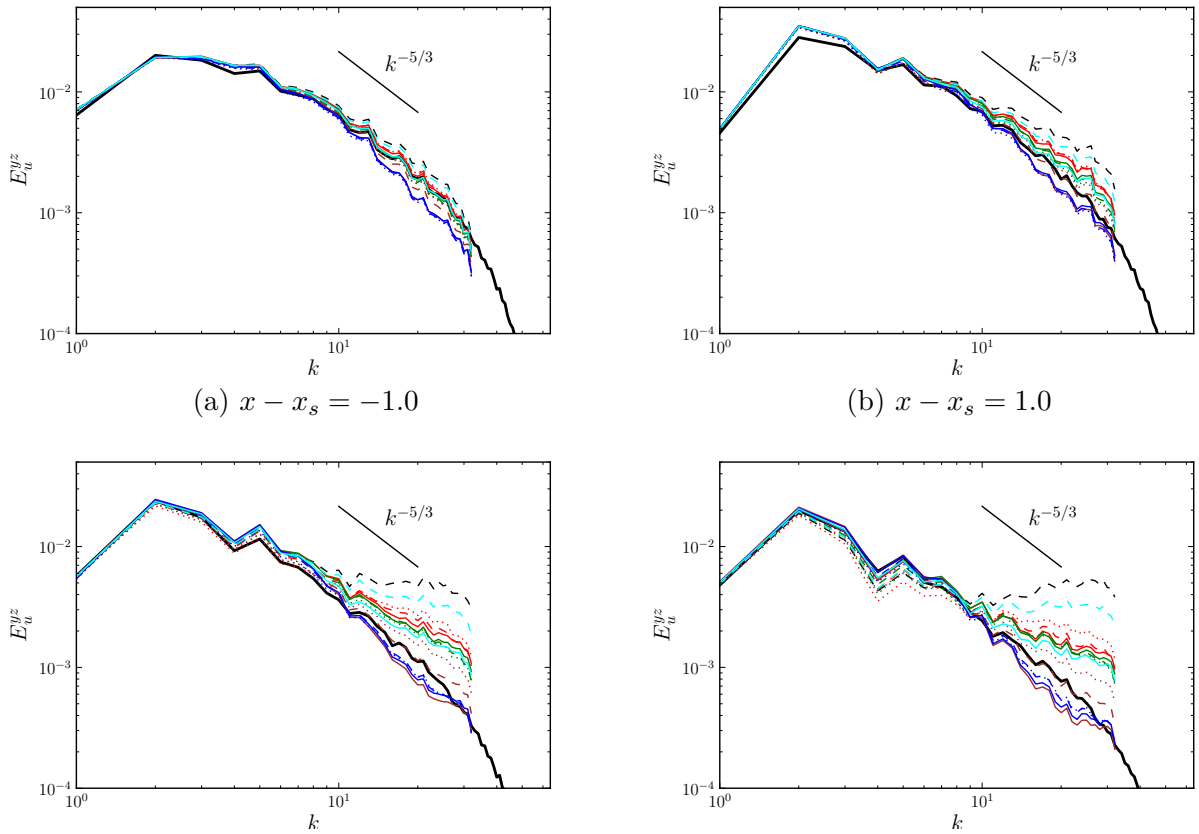

(a) $x - x_s = -1.0$ (b) $x - x_s = 1.0$

(c) $x - x_s = 3.0$ (d) $x - x_s = 5.0$

Figure 11: Streamwise velocity spectra obtained from LES with different models compared to filtered DNS for $M = 1.5$ and grid G1 at four locations relative to the average shock position. Filtered DNS is plotted in solid black and LES with no model in dashed black. The line styles corresponding to the LES with the different implemented models are specified in Table 5.

the shock which are closest to the filtered DNS results. The selection of the mixed term in use has a small effect on the result, for this particular flow. The stretched-vortex model performs better with the orientation model V1, providing a peak value immediately downstream of the shock closest to the filtered DNS, although the subsequent rate of decay is underpredicted (also upstream of the shock).

Results for the normalized transverse Reynolds stress, R_{yy}/R^u_{yy}, show (Figures 9b) worse agreement than for R_{xx}/R^u_{xx}. The best agreement with filtered DNS is provided by mixed models with Vreman's eddy-diffusivity and Lagrangian averaging, even though the value immediately downstream of the shock is still underpredicted. Upstream of the shock, the decay rate of R_{yy} is also best captured by those models. Note that other models result in R_{yy} that are not monotonically decreasing downstream of the shock.

The normalized turbulent kinetic energy, TKE/TKE^u, shown in Figures 9c, reflects a consistent underprediction of the amplification occurring immediately after the shock, due to the underpre-

diction of R_{yy}. This is compensated by the overprediction of R_{xx} farther downstream, recovering the proper rate of decay. Models with Vreman's eddy-diffusivity provide the best results.

Overprediction of R_{xx} and underprediction of R_{yy} downstream of the shock, described above for all models, result in levels of anisotropy (R_{yy}/R_{xx}) that differ significantly from the filtered DNS data (Figure 9d). Note that even upstream of the shock there is a lack of agreement. As before, models with Vreman's eddy-diffusivity show better results.

Figure 10 shows results obtained by doubling the resolution in the streamwise coordinate (grid G2), for $M = 1.5$. The finer streamwise grid has the greatest impact in R_{yy} which reproduces the results of the filtered DNS more accurately (Figure 10b) than for grid G1, particularly in the region immediately downstream of the shock. This could indicate that high streamwise-wavenumbers contain motions primarily leading to transverse Reynolds stresses. As a result, the profiles of TKE and Reynolds stress anisotropy (Figure 10c,d) follow the filtered DNS results more closely. Again, the best results are obtained with Vreman's eddy-diffusivity models. Note, nonetheless, that a Vreman's eddy-diffusivity model with similarity mixed term and transverse plane averaging results in a wrong prediction of turbulence quantities for $x - x_s > 2$, which was traced back to changes in the trend of eddy-diffusivity model coefficients.

Figure 11 shows streamwise velocity spectra computed on transverse planes at four streamwise locations relative to the average shock position ($x - x_s = -1.0, 1.0, 3.0, 5.0$), for all LES models on grid G1, compared to filtered DNS and no-model LES (which acts as an upper bound). Upstream of the shock, Vreman's eddy-diffusivity models appear to dissipate slightly more energy than that required in the resolved part of the inertial range, particularly when Lagrangian averaging is used. After the shock, an energy transfer to the low-wavenumber part of the spectra occurs for all models. Pile-up of the spectra at high wavenumbers is noticeable at $x - x_s = 1.0$ for most models, increasing downstream, except for mixed Vreman's eddy-diffusivity models with Lagrangian averaging and the pure Vreman's eddy-diffusivity model with transverse plane averaging, whose spectra remain close to the filtered DNS and below them for the majority of wavenumbers.

Figure 12 shows streamwise profiles of turbulence-related quantities for the case with $M = 3.5$ and grid G1. Errors in the amplification of normal Reynolds stresses increase with respect to the $M = 1.5$ case: R_{xx}/R^u_{xx} is more overpredicted and R_{yy}/R^u_{yy} is more underpredicted immediately downstream of the shock. These two effects cancel out in the TKE/TKE^u, obtaining reasonable agreement with filtered DNS at both Mach numbers, but add up, on the other hand, in the prediction of Reynolds stress anisotropy, which worsens for the larger Mach number. Consistently with the lower M case, the best results are provided by Vreman's eddy-diffusivity models. Note the increase in SGS dissipation immediately downstream of the shock provided by the Lagrangian averaging compared to the transverse plane averaging from $M = 1.5$ to $M = 3.5$ (Figures 9e and 12e).

4.4.1 Impact of the order/directionality of WENO scheme and conditional SGS

The results presented so far were obtained with a seventh-order accurate WENO scheme applied only in the streamwise direction near the shock. In addition, SGS models were not applied in regions where WENO was active. This subsection evaluates the effect of 1) modifying the order of accuracy of the WENO scheme, 2) applying WENO also in the transverse directions (common in more complex flows where the shock orientation is unknown or might involve multiple coordinate axes), and 3) applying SGS everywhere.

Figure 13 shows turbulence-related quantities for LES performed with the Lagrangian-averaged

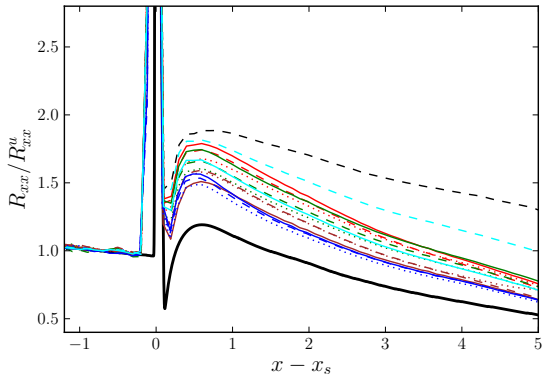

(a) Normalized streamwise Reynolds stress

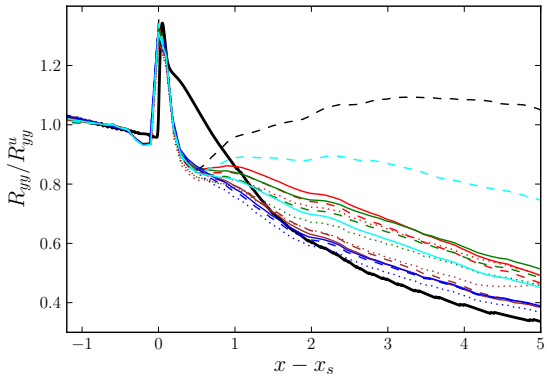

(b) Normalized transverse Reynolds stress

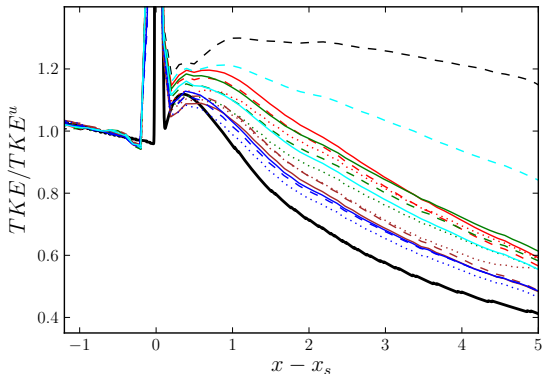

(c) Normalized turbulent kinetic energy

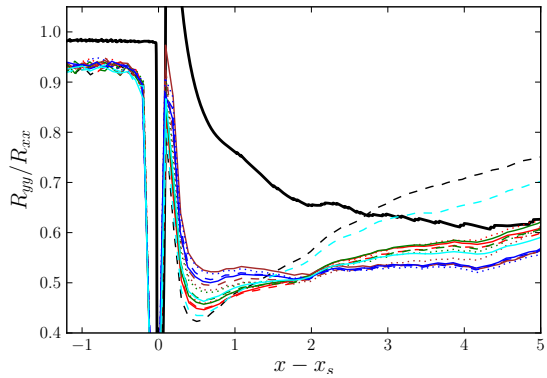

(d) Reynolds stress anisotropy

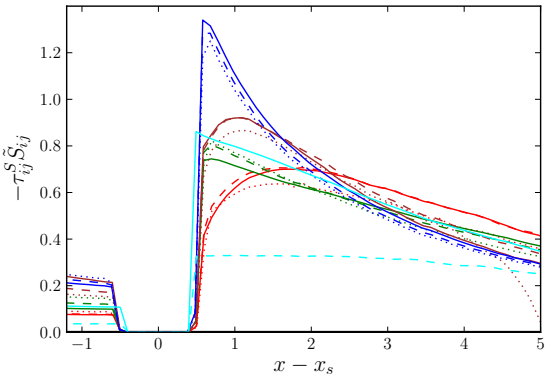

(e) Subgrid-scale dissipation

Figure 12: LES results for $M = 3.5$ and grid G1. Filtered DNS, solid black; no-model LES, dashed black. See Table 5 for SGS-LES line styles.

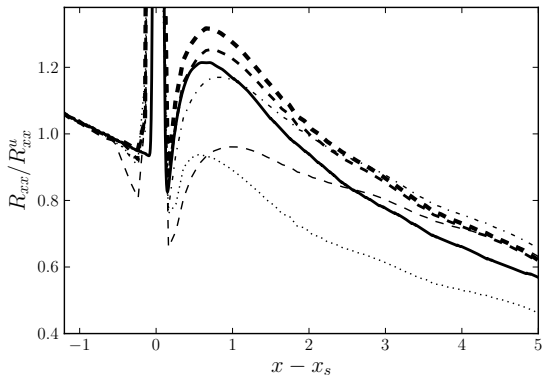

(a) Normalized streamwise Reynolds stress

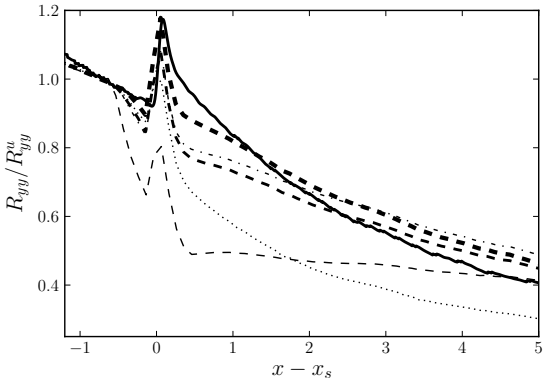

(b) Normalized transverse Reynolds stress

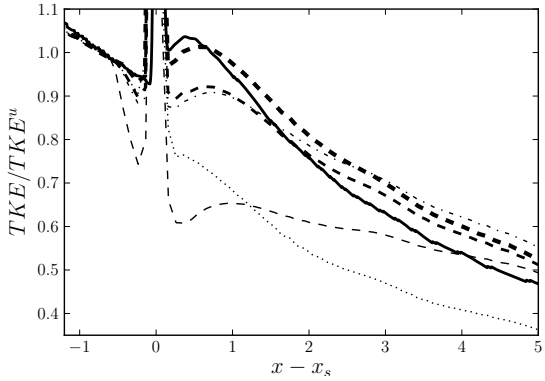

(c) Normalized turbulent kinetic energy

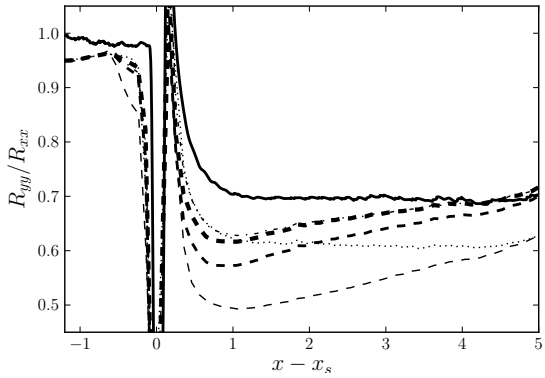

(d) Reynolds stress anisotropy

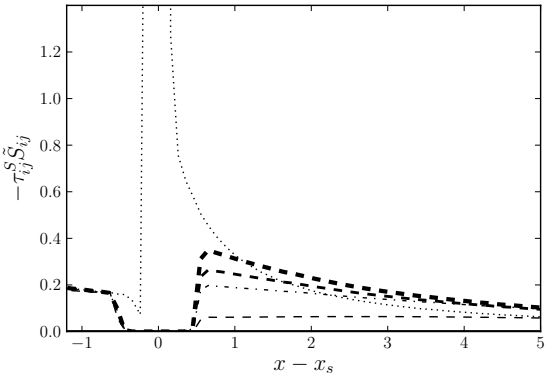

(e) Subgrid-scale dissipation

Figure 13: LES and filtered DNS results for $M = 1.5$ and grid G1 with the Lagrangian-averaged dynamic Vreman's eddy-diffusivity model. Filtered DNS, solid line; LES with third-, fifth- and seventh-order WENO schemes applied only in the streamwise direction near shocks and conditional SGS (only applied where WENO is not active) are plotted in dashed lines of thickness increasing with the WENO order of accuracy; LES with seventh-order WENO scheme applied in the three coordinate directions and conditional SGS is plotted in dash-dotted line; LES with seventh-order WENO scheme and SGS model applied everywhere is plotted in dotted line.

dynamic Vreman's eddy-diffusivity model (MNVL) and different variants of WENO schemes, directionality and conditional SGS application. The order of accuracy of the WENO scheme plays a decisive role in the amplification of turbulence across the shock and its downstream evolution, at this grid resolution. The results obtained with a third-order WENO compare poorly with filtered DNS: in particular, instead of the expected amplification of R_{yy} after the shock and its monotonic decrease downstream, their values are significantly reduced immediately after the shock, remaining almost constant farther downstream. Fifth-order WENO improves substantially the results: even though there is still no amplification of R_{yy} after the shock, the monotonic decrease downstream is better reflected, approaching the correct value at $x - x_s = 5$. R_{xx} is also significantly improved. Seventh-order WENO provides better results, particularly for R_{yy} and TKE. These three cases applied WENO only in the streamwise coordinate direction.

The additional damping obtained when seventh-order WENO is applied in all three coordinate directions (dash-dotted line in Figure 13), instead of only in the streamwise direction, is more noticeable for R_{xx} than for R_{yy}. The transverse Reynolds stress and TKE are comparable to those obtained with a fifth-order WENO applied only in the streamwise direction, although the decay rate farther downstream is more underpredicted.

When the SGS model is applied everywhere, the extra SGS dissipation added in WENO regions (see dotted line in Figure 13e) considerably damps the turbulence across the shock. R_{xx} levels are comparable to those obtained with a third-order WENO, whereas R_{yy} lies between a third- and a fifth-order WENO. The rate of change downstream follows the filtered DNS results, but the absolute values are considerably lower.

5 Shock-turbulence interaction in spherical geometry

The canonical problems of shock-turbulence interaction and Richtmyer-Meshkov instability (RMI) are central to understanding the hydrodynamic processes involved in Inertial Confinement Fusion (ICF). Over the last few decades, there has been considerable analytical, computational and experimental work on the planar versions of these problems. In spite of the problem of interest being spherical in nature, there have been almost no studies in any of the three areas for these problems. It is not clear a priori, that the conclusions drawn from their planar versions carry over to the spherical domain. The research presented in this section represents a first attempt to understand the hydrodynamic processes involved in an Inertial Fusion Engine (IFE) from capsule implosion to interaction of the resulting shock waves with the chamber gases. To abstract the key hydrodynamic components from the complex physics involved in an IFE, three canonical problems are identified and simulated: interaction of a blast wave with isotropic turbulence, interaction of a converging shock with isotropic turbulence and RMI in spherical geometry. The last problem is a hydrodynamic abstraction of the capsule implosion itself, while the first two problems attempt to model the late stage interaction of fusion induced shock waves with chamber gases.

5.1 Interaction of a converging shock wave with isotropic turbulence

5.1.1 Isotropic Turbulence

The turbulence here is taken to be isotropic turbulence in a periodic box, as this is one of the most well understood forms of turbulence. The turbulent field is one of decaying isotropic turbulence with eddy shocklets. The parameters characterizing this field are the turbulence Mach number $M_{t,0}$

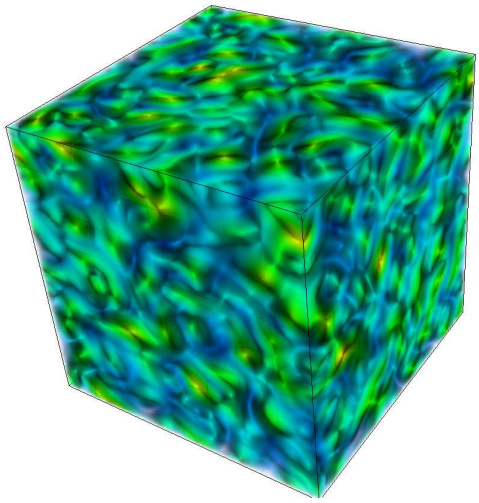

Figure 14: Volume rendering of isosurfaces of vorticity for isotropic turbulence. Simulation domain is 256^3.

and the Taylor scale Reynolds number $Re_{\lambda,0}$. Before launching the shock, the turbulence is first allowed to evolve to a state where the nonlinear energy transfer mechanism becomes fully active. This is indicated by the velocity derivative skewness attaining a steady negative value. The time at which the enstrophy is at its peak, indicating that the vortical fluctuations are at their greatest before viscosity starts dissipating them is selected as the time to launch the shock. This occurs at about $t = 1.5\tau_0$, where τ_0 is roughly the eddy turnover time.

Taylor scale Reynolds number of the flow Re_λ is 45 and the turbulent Mach number M_t is 0.4. The turbulence field can be considered to be weakly compressible. This value of M_t is however high enough to form eddy shocklets that persist up to late times.

5.1.2 Converging shock

A schlieren wave diagram for the converging pure shock problem elucidates the driving flow. This is shown in figure 15. At the time of shock launch, one can observe two fronts, the shock wave propagating radially inwards and the expansion wave traveling outwards. Note the absence of a contact surface due to appropriately chosen shock tube parameters. The shock gets progressively stronger as it approaches the origin at which point, it is at its strongest. It then reflects off of the origin and propagates outwards. The expansion wave propagates outwards and interacts with the buffer layer where windowing is applied. This layer absorbs the wave with no reflections or transmission from neighboring periodic images. Pressure and density achieve very large values as the converging shock nears the origin which leads to large gradients. Additionally, the shock is relatively poorly resolved near the origin compared to the rest of the domain. This results in higher numerical dissipation, which is seen as a diffuse patch in the schlieren plot near the origin. Radial velocity decays linearly to zero at the origin in the reflected shock regime.

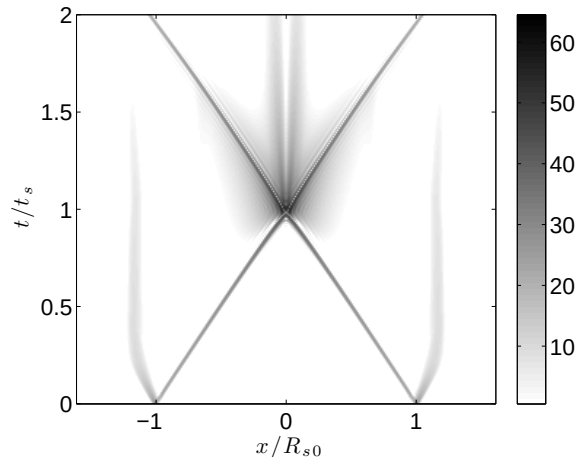

Figure 15: Density schlieren wave diagram for converging pure shock. Quantity plotted is $10\log|\nabla\rho|$. Shock initial Mach number $M_{s0} = 1.4$. t_s is time taken for shock to reach the origin, i.e. $t_s = t_{R_s=0}$.

5.1.3 Converging shock-turbulence interaction

We now add the two components described earlier to generate a spherical shock propagating through a field of isotropic turbulence. The converging shock starts out relatively weak, but gains strength as it propagates inwards. The Taylor scale Reynolds number Re_λ is 45 and the turbulent Mach number M_t is 0.4. The shock is captured by 4 grid points, a characteristic of the artificial viscosity method employed here (see (17)), giving a shock thickness $l_s = 3\Delta$ and a shock thickness to turbulence length scale ratio l_s/l_0 of 0.05, i.e the shock length scale is much smaller than turbulence. All shocks including eddy shocklets in the isotropic turbulence field are captured, and not resolved.

A shock time scale is computed based on the time it takes for its pressure ratio to increase to twice its value and this is compared with the turbulence time scale τ_0. For the weakest converging shock, $\tau_s/\tau_0 \sim 1$, while for the strongest, $\tau_s/\tau_0 << 1$, so the assumption of frozen turbulence is only valid for the strong shock case.

The Kolmogorov scale, the smallest length scale in the flow, below which dissipation takes over, initially *decreases* behind the shock and remains lower than the pre-shock value. These scales are slightly underresolved in our 256^3 simulations. We have conducted a grid-resolution study to establish that the numerical results for turbulence statistics are essentially grid-independent.

Vorticity dynamics Figure 35 shows slices vorticity magnitude at midplane for the converging shock. Vorticity is amplified by the flow following the expanding shock. The reason for this is that the vorticity dilatation term, $-\omega(\nabla \cdot u)$, which acts as a source of vorticity in regions of negative dilatation, such as the one following a converging shock. The overall effect of the converging and reflected shocks is a decrease in size of the eddies, as can be seen in figure 35, which plots slices of vorticity magnitude along the midplane. Plot 35(a) shows the vorticity field before shock launch and plot 35(b) shows it at a late time, $t/\tau_0 = 0.9$ when $R_s/R_{s0} \sim 1$, i.e the reflected shock is almost out of the domain. Smaller scale structures in the post reflection plot can be noted.

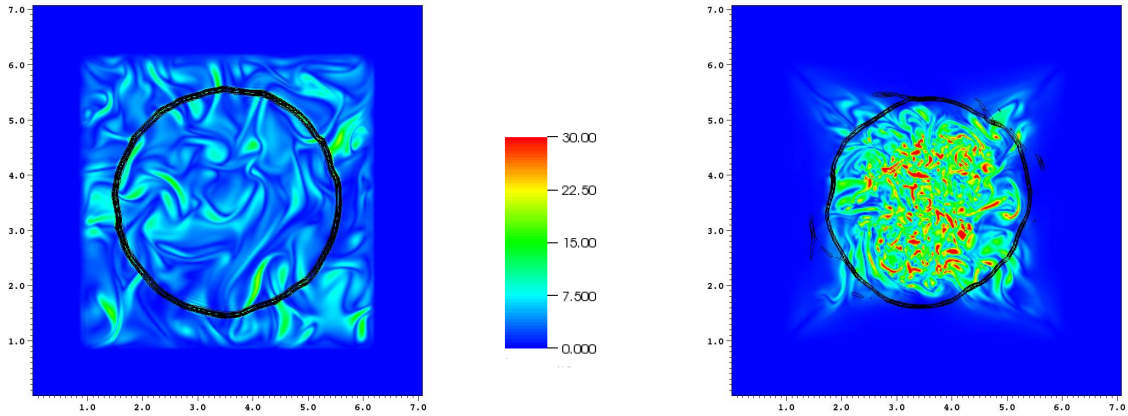

(a) (b)

Figure 16: Slices of total vorticity superimposed on dilatation contours showing shock location at mid plane for (a) Converging shock at $t/\tau_0 = 0$, (b) Reflected shock at $t/\tau_0 = 0.9$ for case C2G288.

Time evolution of the shock We seek to understand the effect of the turbulence on shock evolution and compare it with the case with no background turbulence. In absence of turbulence, the shock is nominally spherical. Turbulence distorts this sphericity depending on its relative strength compared to the shock. As also described in (18), we define a shock asphericity parameter χ based on the shock radius.

Figure 17 shows these quantities for the converging shock at $M_{s0} = 2.4$. The shock radius deviates considerably from the pure shock case, which as noted in §5.1.2 follows Guderley's scaling for a converging shock.

This is seen in the asphericity which starts out higher than the pure shock case. The reason for initial asphericity is that the shock is initialized to have the same Mach number at all points that define the initial shock radius. However, due to fluctuations in local density and pressure, the local speed of sound is different at these points. Consequently, local shock speed is different and the shock therefore starts out aspherical. A strong shock, as it propagates inward, strengthens rapidly and does not acquire further asphericity due to interaction with turbulence. A weaker initial shock on the other hand, acquires further asphericity until it becomes strong enough not to be affected by surrounding turbulent fluctuations. This is seen in figure 18, which compares slices of pressure contours during the converging phase of the shock at the same mean shock radius ($R_s/R_{s0} \sim 1/2$) for different initial shock Mach numbers. The stronger initial shock retains retains only the initial distortion, while the weaker initial shocks are relatively more aspherical.

5.1.4 Maximum compression

We also compare the maximum compression achieved by the converging shock in presence and absence of turbulence. One would expect that for a shock propagating through turbulence, the maximum compression achieved would be less than for a pure shock with the same initial Mach number. We are interested in the magnitude of this decrease in maximum compression and how is

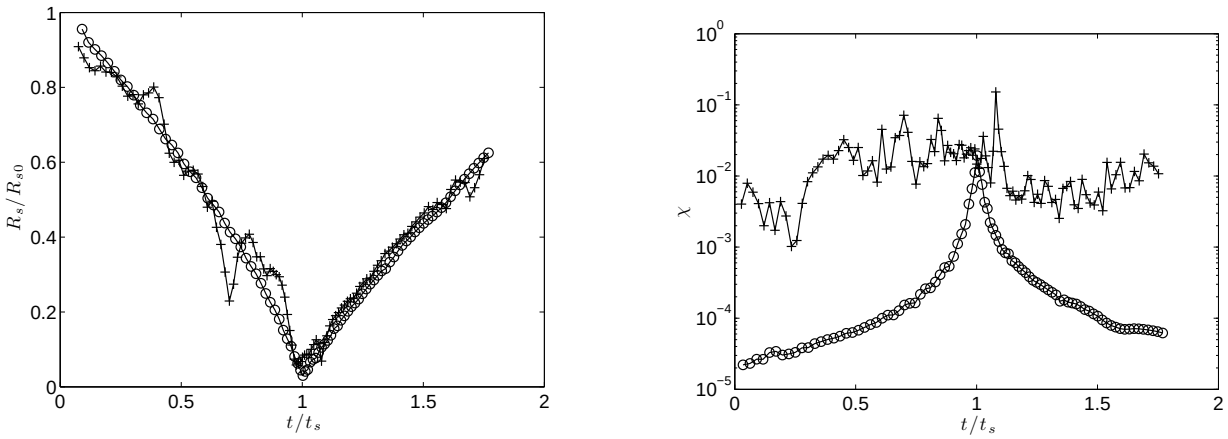

(a) (b)

Figure 17: Evolution of (a) Shock radius and (c) Shock asphericity, for converging (Case C2G288). Shock with Turbulence (+ symbol), Pure shock (o symbol)

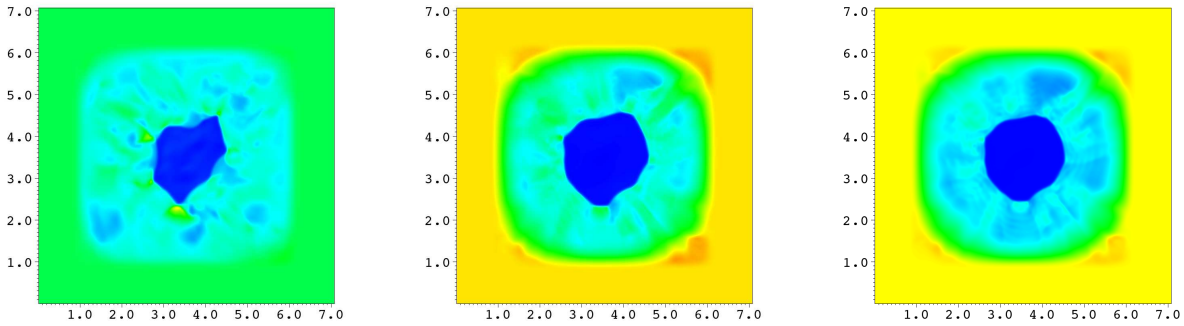

(a) (b) (c)

Figure 18: Slices of pressure contours during the converging phase at (a) $M_{s0} = 1.4$ (Case C1G288), (b) $M_{s0} = 2.5$ (Case C2G288) and (c) $M_{s0} = 4.0$ (Case C3G288) at different times but same mean shock radius, $R_s/R_{s0} = 0.45$. Contour levels are *not* same across plots.

M_{s0}	Pure shock		Shock-Turbulence	
	ρ_{max}/ρ_0	P_{max}/P_0	ρ_{max}/ρ_0	P_{max}/P_0
1.4	14	72	9	29
2.4	40	781	34	422
4.2	65	2496	57	1696

Table 6: Comparison of pressure and density ratios at maximum compression for a pure shock with shock propagating through turbulence

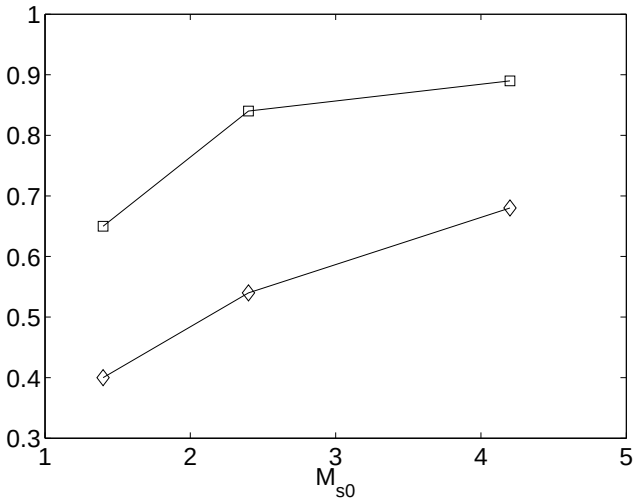

Figure 19: Pressure and density ratios at maximum compression in presence of turbulence compared to pure shock case. Quantities plotted are $(\rho_{max}/\rho_0)_{shock-turbulence}/(\rho_{max}/\rho_0)_{pure-shock}$ ($\square$ - symbol) and $(P_{max}/P_0)_{shock-turbulence}/(P_{max}/P_0)_{pure-shock}$ ($\diamond$ - symbol)

it affected by initial shock Mach number.

Table 6 tabulates maximum density and pressure ratios at different Mach numbers for pure shock and shock with turbulence cases. As expected, these increase with increasing shock strength. Figure 19 plots the maximum pressure and density ratios as a percentage of their highest values for the corresponding pure shock cases. It is seen that the decrease in maximum compression is greatest for the lowest Mach number case (65% for density and 40% for pressure compared to pure shock case) and tends to level off for stronger initial shocks (90% for density and 70% for pressure). This is expected, since stronger shocks are less distorted by turbulence and therefore remain more symmetric as they propagate inwards and consequently are able to compress the fluid more effectively.

6 Shock-accelerated mixing

The Richtmyer-Meshkov (RM) instability occurs when a shock wave impulsively accelerates a material interface. Misalignments between the pressure jump in the shock and the density jump

across the (slightly perturbed) material interface cause baroclinic generation of vorticity, which subsequently begins mixing the two materials. This phenomenon is of practical interest in inertial confinement fusion, where the growth of the initial RM instability seeds later Rayleigh-Taylor instabilities with adverse effects on the implosion process. The objective of the work presented in this section is to study the physics of nonlinear RM mixing and to develop improved models. We take a two-step approach involving first the study of the planar geometry (also including shock-curtain interaction) and moving later to the spherical case, that will use the insight acquired through the analysis of shock-turbulence interaction in such geometry.

6.1 Planar Richtmyer-Meshkov mixing

In the experiment of Vetter and Sturtevant (19), a Mach 1.5 shock impinged upon an interface between air and SF6. A regular wire mesh containing a membrane was used to separate the two fluids initially. Since a closed shock tube was used, the incident shock reflected from the end of the shock-tube and re-shocked the evolving interface. Following reshock a very complex, turbulent flow was observed in the domain.

The thermodynamic conditions in the experiment are matched in our simulations. The experiment used a wire mesh with 28 intervals along each direction and a membrane to initially separate the two fluids. In the computations the initial interface is a linear combination of a regular egg-carton perturbation and a much smaller irregular perturbation to seed chaotic motions, with 4, 8 or 14 egg-carton intervals in each direction. Presently, we have performed computations on grids with transverse resolutions of 128^2 (coarse) and 256^2 (medium) points. The number of grid points in the shock-normal direction is approximately 2.5 times higher than in the transverse direction. The results shown here correspond to computations carried out using the supercomputing facilities at the National Center for Computational Sciences (NCCS) through their Early Access program.

6.1.1 Mixing Zone Width

The total mixing width is a global measure of mixing between the two fluids. Figure 20 shows the evolution with time of the mixing width for the three different initial condition cases (4, 8, 14 egg-cartons along each direction of the interface), as well as the results from previous numerical simulations of Hill and Pantano (20) and experimental data, for comparison. Exact match with the experimental data should not expected, primarily due to the uncertainty about the exact initial interface in the experiments. Nonetheless, we observe a good agreement of the growth rate of the interface. As time progresses, the "bubbles" and "spikes" in RM mixing merge and become larger; this explains the dependence on the initial condition at late times, where the cases with fewer initial wavelengths present become limited by the size of the computational box.

6.1.2 Spectra of scalar variance

The scalar mass fraction is related to the mixing process. Figure 21 shows spectra of its variance in the transverse directions at two different times. Immediately after re-shock, the spectra are peaked primarily at the dominant wavenumber in the initial condition. This shows how the flow still retains its original characteristics. At later time, when the flow has become fully turbulent, the scalar mass fraction is instead very broadband without any dominant peaks. A $k^{-5/3}$ range is visible in the spectra, followed by a sharp drop-off due to the numerical dissipation.

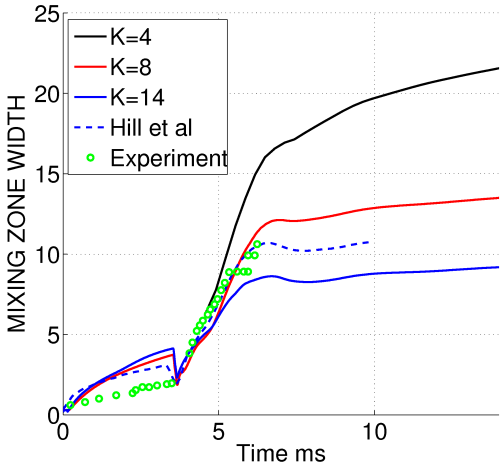

Figure 20: Growth of the mixing zone in planar Richtmyer-Meshkov mixing.

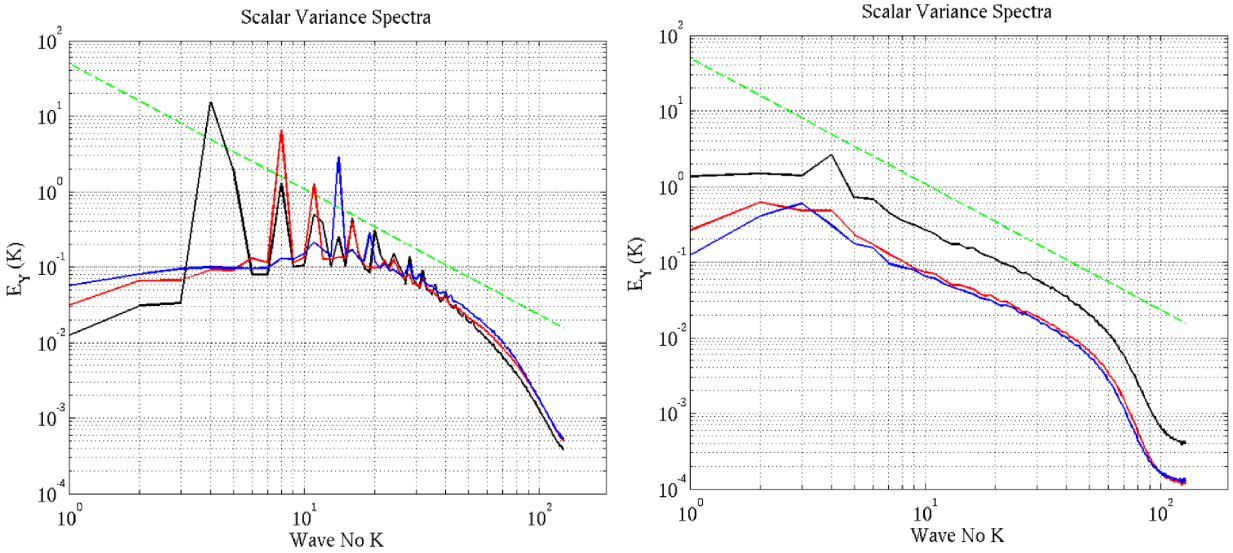

Figure 21: Two dimensional spectra of scalar variance just after re-shock (5ms) (left) and at late times (14ms) (right). Dotted green line indicates the $-5/3$rd slope. See figure 20 for color reference.

6.1.3 Interface

Figure 22 shows qualitative plots of the interface at three different time instants resulting from an initial condition with 8 egg cartons along the cross-sectional directions. Cross-sectional cuts at planes $Y = \pm 4.5$ are also shown in that figure for each instant in time. At $t = 4.5$ ms (just after re-shock) the remains of the 8 egg cartons are still visible, as indicated by the presence of 8 bubble-spike-like structures. At later times the flow appears more mixed (turbulent mixing) and there is no visual trace of bubble-spike-like structures. This is consistent with the spectra discussed above,

in that the mixing zone retains a "memory" of the initial condition until shortly after re-shock.

6.2 Shock-curtain interaction

Moderate and high-resolution three dimensional numerical simulations of a shock interacting with a curtain of dense gas are carried out using the FDL3DI-SU code. The flow is initialized in three regions: a post-shock region of air, an ambient region of air and a curtain of heavy gas in the ambient region. The thermodynamic state of the fluids in the flow domain is shown in Fig 23. The concentration profile in the curtain region is given by the Mikaelian fit indicated in Fig. 24 where the parameters (A,B,β,α,κ) are assumed to be Gaussian random variables with mean (0.7,0.2,-0.04,0.836,1.745) and standard deviation (5,5,10,0.5,0)% of mean. These are the values reported in the experiment (21) except that the standard deviation of κ is assumed to be zero, to maintain the periodic boundary condition in the cross-sectional plane. A sample line cut of $\phi_{HeavyGas}$ through the X and Z is shown in Fig. 24. Time is initialized to zero when the incident shock meets the interface. A case of reshock is also studied, where the incident shock reflects off the end wall and reimpacts the interface at $\sim 600\mu s$.

The heavy gas is a mixture of SF_6 and *acetone*. The effect of *acetone* (used as a tracer species for PLIF visualization purpose) on the flow is found to be non-negligible (24). In this study we account for the presence of all the three species-*air*, SF_6 and *acetone*. Molecular viscosity μ_i of the pure species are computed using the Chapman-Enskog equation (similar model is used for mass diffusivity D_i and thermal conductivity k_i). The molecular properties of the fluid mixture are calculated using Wilke mixing model (for μ and k) and the Ramshaw self-consistent effective diffusivity model (for D).

The accurate characterization of the absolute concentration levels of the species in the heavy gas mixture at the initial conditions in the experiments is a challenging task and reliable data of the same are not available. Three simulations with different peak concentration levels of the heavy gas mixture are conducted. SF_6 and *acetone* composing the heavy gas are assumed to be well mixed and have the peak mass fraction values of (0.80, 0.14), (0.70, 0.14) and (0.70, 0.10). Higher concentration levels of the heavy gas mixture cause larger vorticity deposition on the interface following the shock impact, leading to a larger instability growth rate. The measure of the curtain width with time shown along with the experimental data (21) in Fig. 6.2(a) (before reshock) and Fig. 6.2(b) (after reshock) exhibits this trend. The numerical simulation corresponding to (0.70, 0.14) is seen to be in good agreement with the experimental data. The following results will correspond to this case. Results are non-dimensionalized by using a reference length scale $l_{ref} = 1mm$ and a reference velocity scale $u_{ref} = a^o_\infty$(upstream sound speed).

Temporal evolution of the iso-surface of the heavy gas mass fraction is shown in Fig. 6.2. Vorticity deposited by the initial shock impact causes counter rotating vortex pairs to be formed which result in the mushroom-like shapes (Fig. 6.2(a),(b)). Re-shock at $635\mu s$ deposits higher energy into the non-linear flow-field causing the large scale structures to break up and resulting in a chaotic flow-field at late times (Fig. 6.2(c),(d)).

The fluctuating velocity field is defined as: $u_i\prime(x,y,z,t) = u_i(x,y,z,t) - \langle u_i(x,t)\rangle$ where the average velocity field is the velocity averaged over the cross section: $\langle u_i(x,t)\rangle = \int_{-L_y/2}^{L_y/2}\int_{-L_z/2}^{L_z/2} u_i(x,y,z,t)dydz$. A measure of the turbulent kinetic energy given by $TKE = \langle u\prime_i u\prime_i\rangle$ is plotted in Fig. 27. Following the initial shock impact the TKE in the domain shows a slow decay and a double peak structure after re-shock followed by a rapid decay of TKE. The fluctuating velocity field is characterized by

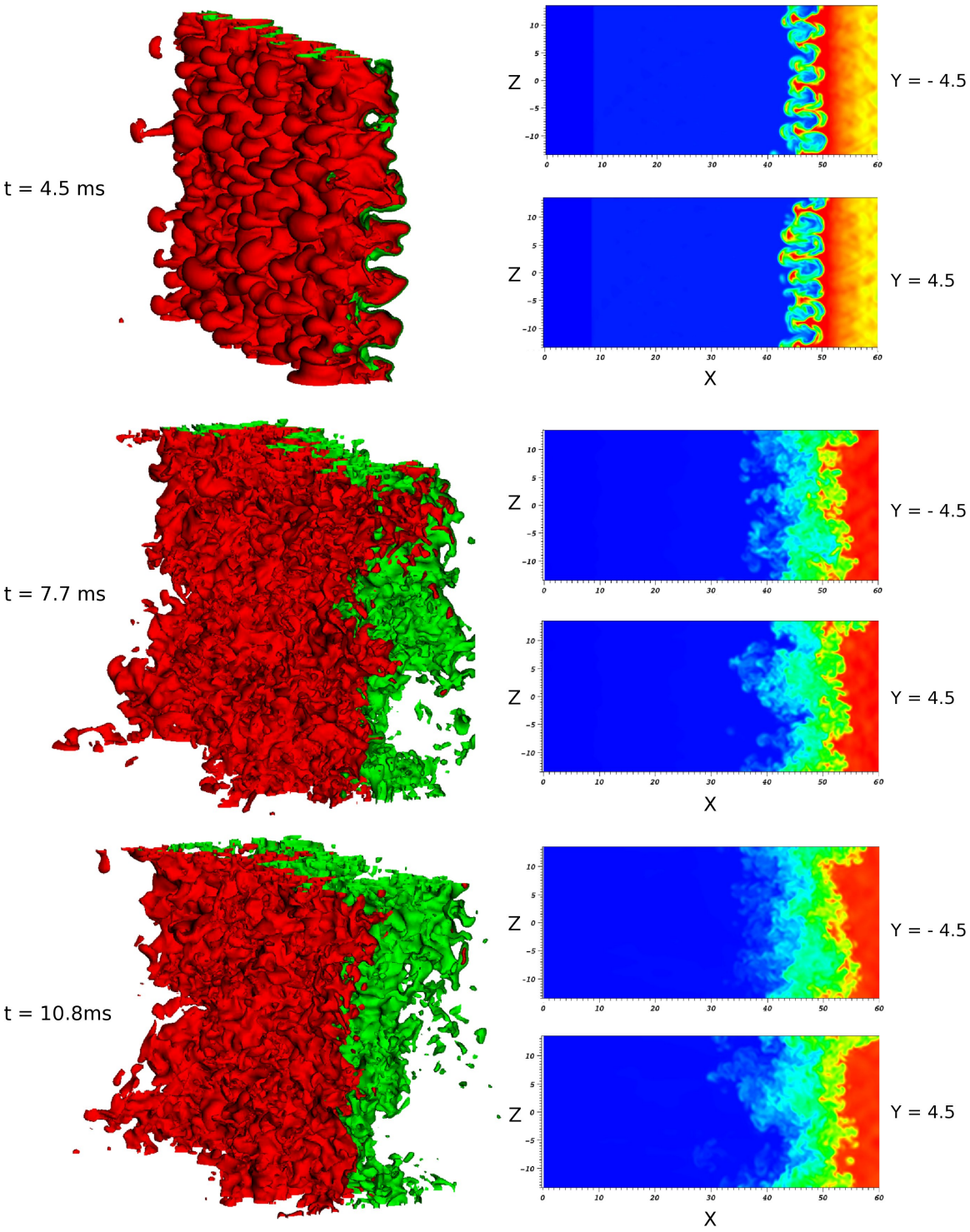

Figure 22: Left: three-dimensional iso-contours of density at three different time instants (top, center and bottom) after initial shock impact, for an initial condition corresponding to $K = 8$. Right: $X - Z$ plane cuts of density at locations $Y = \mp 4.5$ for each time instant.

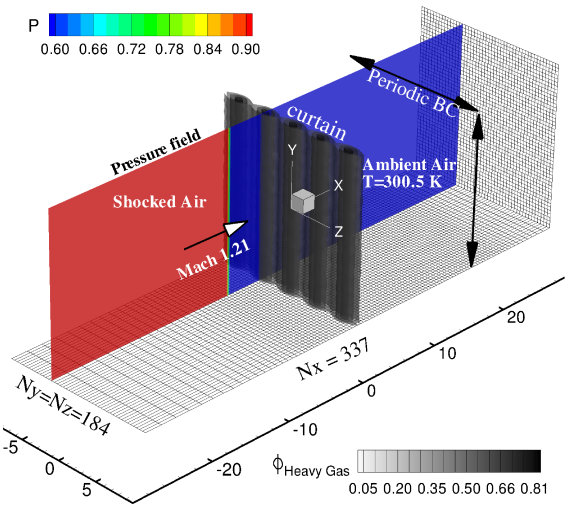

Figure 23: Initial conditions

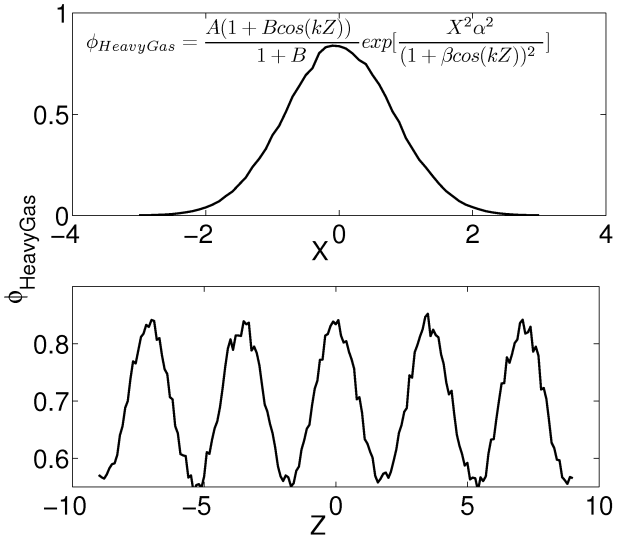

Figure 24: Mass fraction of heavy gas across curtain

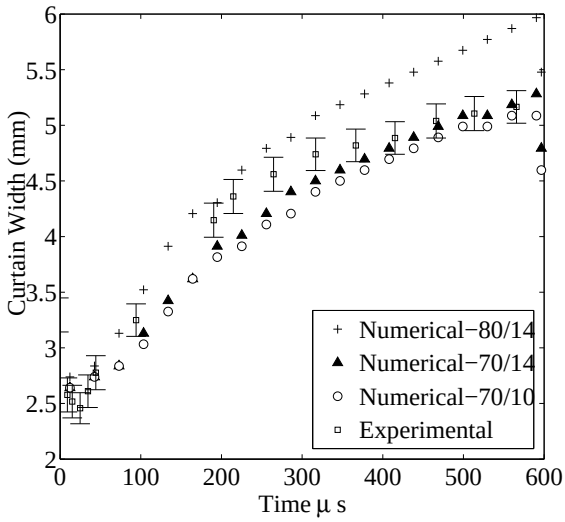

(a)

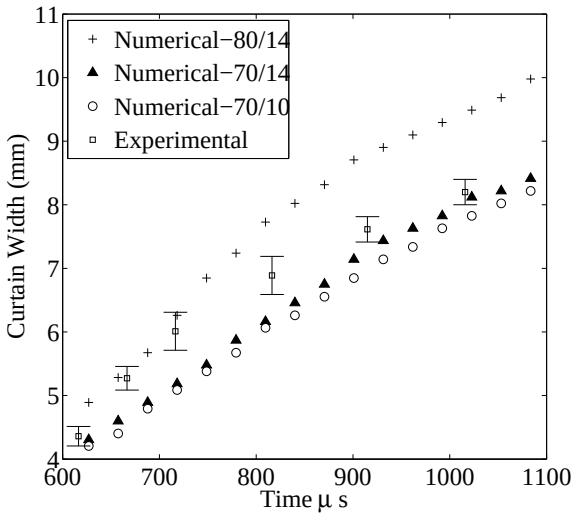

(b)

Figure 25: Temporal evolution of curtain width (**a**) before and (**b**) after reshock

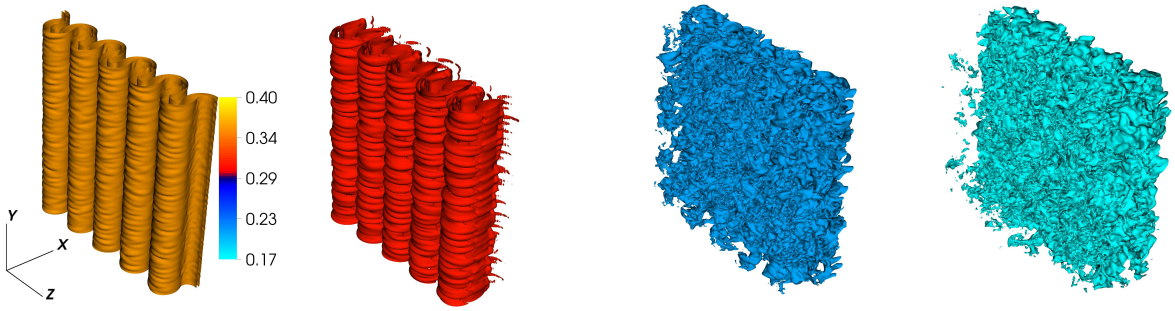

(a) (b) (c) (d)

Figure 26: Time evolution visualizing at iso-surface of $\phi_{HeavyGas}$=45% $\phi^{Max}_{HeavyGas}$ colored by the value at time (**a**) 152 (**b**) 547 (**c**) 943 (**d**) 1247 μs

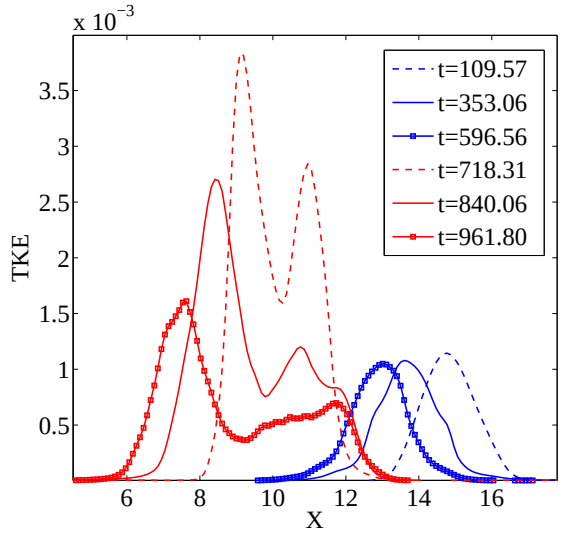

Figure 27: Evolution of turbulent KE before (blue) and after (red) re-shock

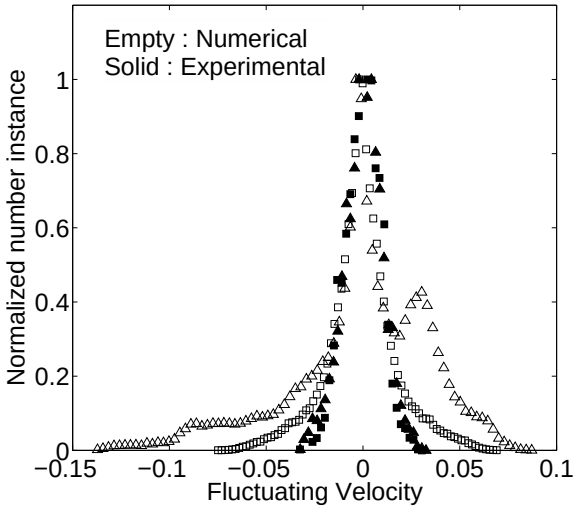

Figure 28: Histogram of fluctuating streamwise (△) and spanwise (□) velocity at t=715μs

the histogram at t$\sim$ 715μs plotted along with the experimental data(21) in Fig. 28. While the span-wise component of velocity shows good agreement with the experimental data, the stream-wise component is seen to have a double-peak structure. This is perhaps due to the fact that the velocity measured in the experiments only records the velocity of the seeded heavy gas while the component of velocity of the surrounding air is ignored while the numerical result takes into account the velocity field in the entire domain (including air and heavy gas).

Hence in the present studies impulsive acceleration of a dense gas curtain in air is investigated by carrying out three-dimensional multi-species compressible Navier Stokes simulation of the flow. The growth of the primary instability is seen to be sensitive to the initial concentration profile of the species present in the flow requiring accurate characterization of the initial flow conditions. The reshock destroys the ordered velocity field present in the flow leading to a transition to turbulent flow causing enhanced mixing of the species present in the flow. Statistics of the fluctuating velocity field from the numerical simulations are compared to experimental measurements.

6.2.1 High resolution simulation

A high-resolution calculation is conducted to investigate in detail the physics underlying the mixing phenomenon. The initial conditions follow the same configuration represented in figure 23. This case had the cross-sectional plane resolved by 552^2 grid points. The total number of grid points in the domain was nearly 500M and the case was run in parallel on 8192 processors.

Isosurface of Q-criterion colored by density

Isosurfaces of the Q-criterion are used to identify vortical structures in the flow, as shown in Fig. 29 and 30 at four different times of the flow evolution. In these figures, red color indicates heavier fluid and blue color indicates lighter fluid. In this simulation the reshock takes place at approximately 600 μs. It is observed that a high degree of anisotropy still remains in the domain for up to 150 μs after reshock. The existence of large scale structures is seen as the presence of the long strands of vorticity in Fig. 29, 52 μs and 103 μs after reshock. At late times (Fig. 30) the uniformity in the colored contours indicate that the fluids are more mixed with each other.

Mixing models: closure for species mass fraction equation

The high-resolution dataset is put to use to test the assumptions made in the BHR mixing model (25), that was developed for variable density flows. The Favre-averaged Navier-Stokes equations are solved and the unclosed terms are modeled by certain approximations. The coefficients in the model have been trained on datasets that were made available from simulations of variable density flows such as Rayleigh-Taylor instability and flows with shear-driven instability. However, lack of robust datasets of RMI prevented calibration of the model for these flows. Using the high resolution dataset of the flow field from the present simulation of RMI, certain modeling assumptions made by the BHR model are tested below.

The Favre-averaged species mass fraction equation of the heavier gas SF_6 (ignoring the molecular

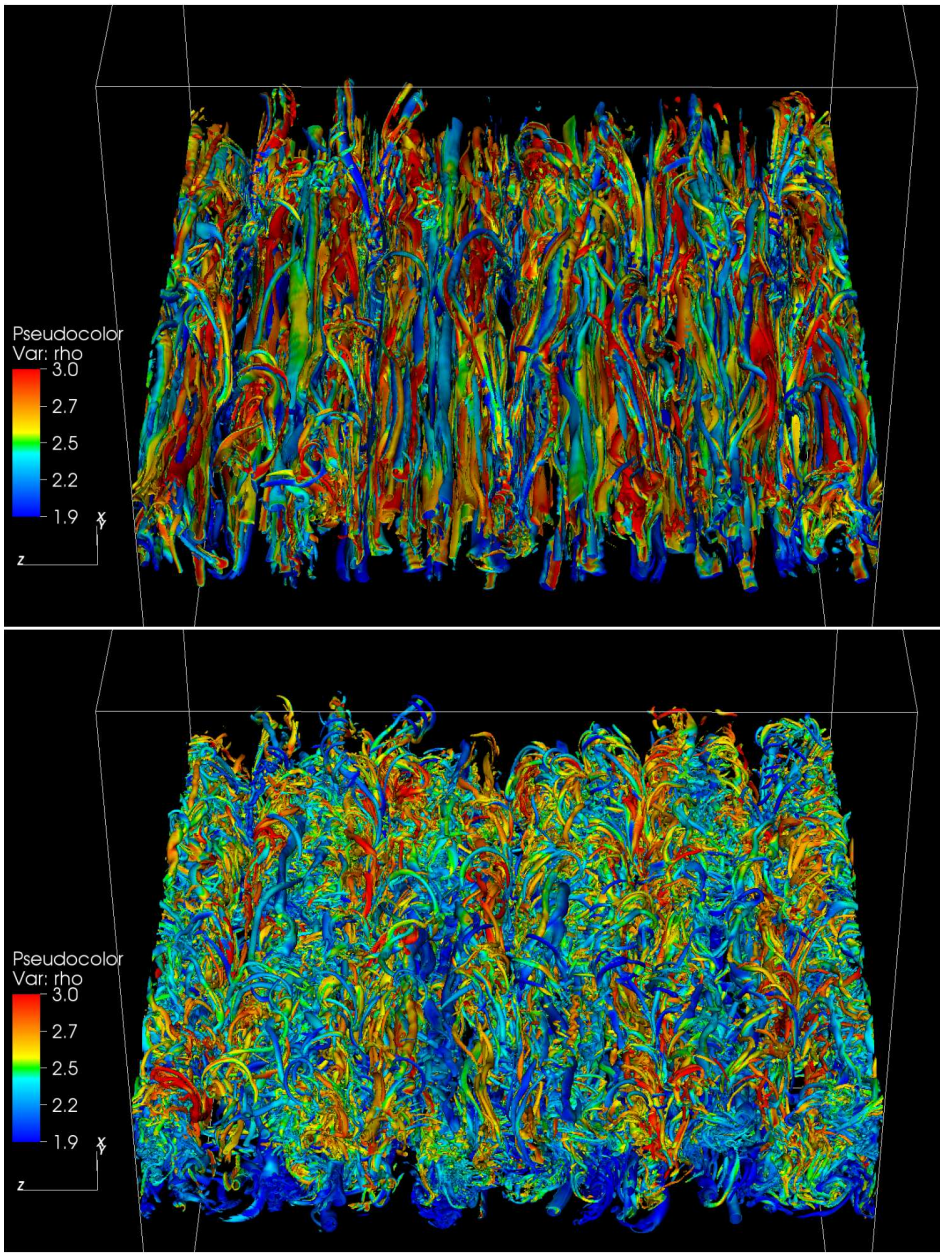

Figure 29: Isovolume of Q-criterion colored by density at times 652 and 703, from top to bottom

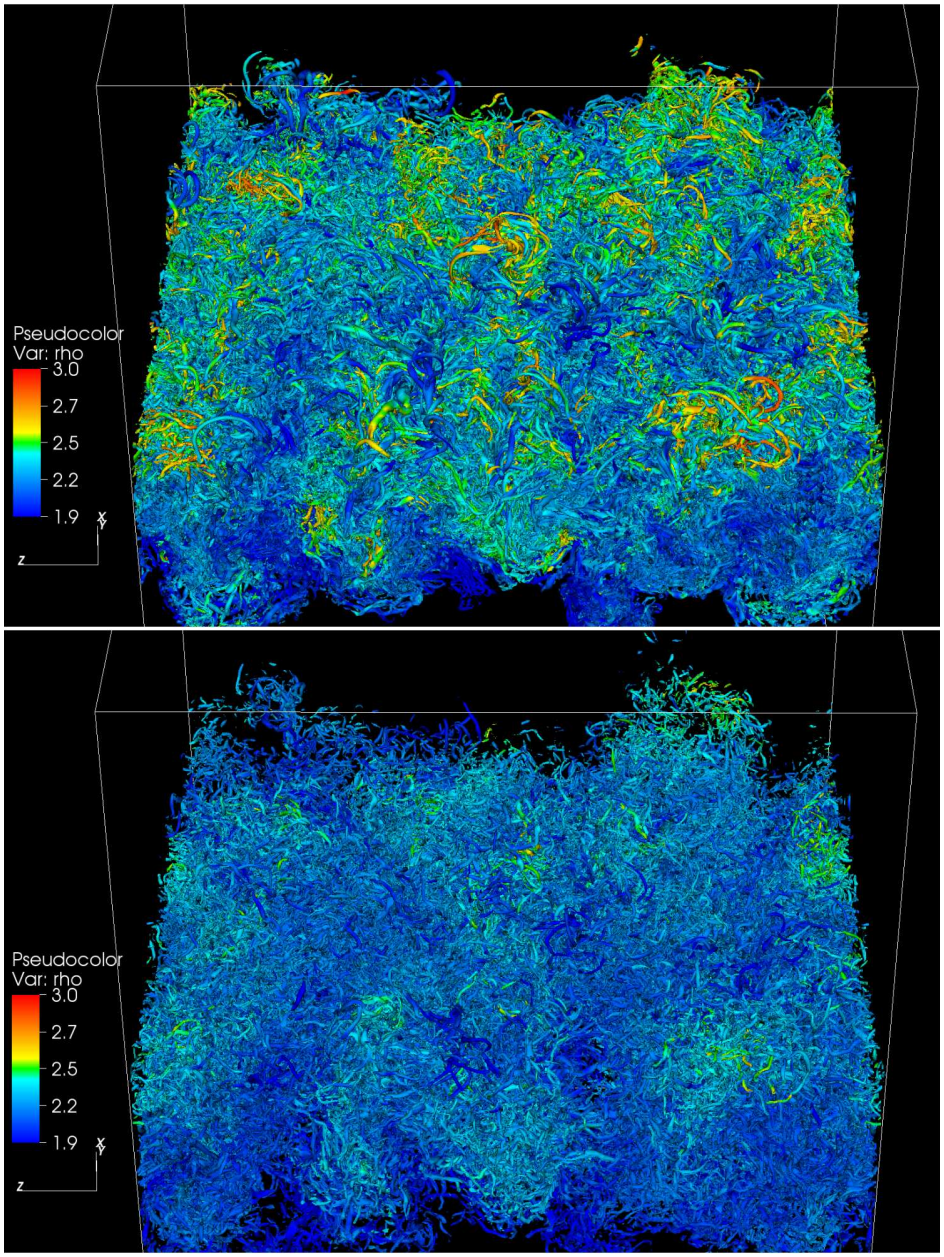

Figure 30: Isovolume of Q-criterion colored by density at times 845 and 1007 μs, from top to bottom

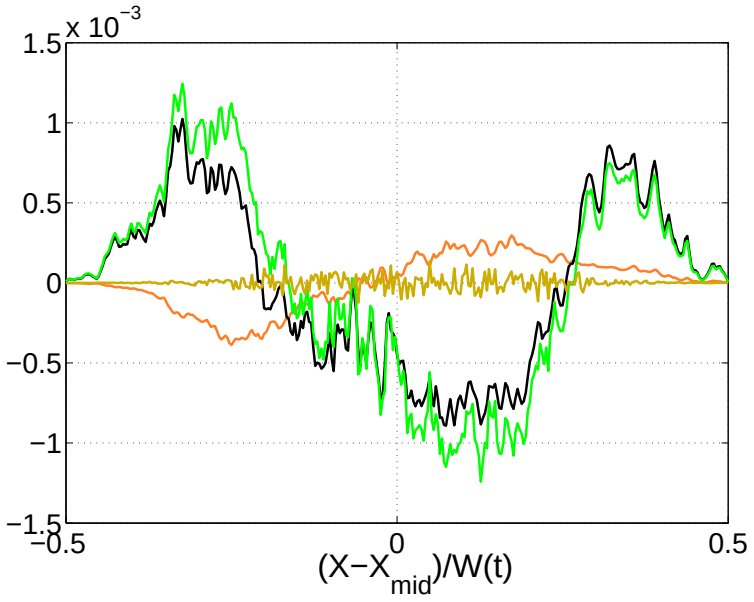

Figure 31: Budget of terms in the Fravre-averaged species mass fraction equation for SF_6 (see equation 6). Black = right-hand-side, yellow = left hand side, which is decomposed into: orange = convective term, and green = temporal term.

transport terms) is given below.

$$\underbrace{\underbrace{\frac{\partial(\bar{\rho}\tilde{Y}_{SF_6})}{\partial t}}_{\textbf{roc}} + \underbrace{\frac{\partial(\bar{\rho}\tilde{u}\tilde{Y}_{SF_6})}{\partial x}}_{\textbf{Cnflux}}}_{LHS} = \underbrace{-\frac{\partial(\overline{\rho u'' Y''_{SF_6}})}{\partial x}}_{\textbf{RHS}} \tag{6}$$

The relative magnitude of the '**RHS**' term compared to the '**Cnflux**' and '**roc**' term is shown in Fig. 6.2.1 at a time t∼1007 μs along the flow evolution. The large value of the '**RHS**' term when compared to the '**Cnflux**' term indicates the importance of modelling it accurately in this flow. This term is comparable to the time rate of change of the species mass fraction. The '**RHS**' term is the turbulent transport of species and requires closure. The yellow curve denotes (LHS-**RHS**) which should be zero in an inviscid flow. The deviation from zero value is attributed to the presence of molecular (and artificial) dissipation and errors associated with calculation of temporal rate of change in an unsteady flow field from two time instances.

The term marked **RHS** is modeled using a gradient diffusion hypothesis. In the BHR model suggested by Schwarzkopf *et al* (25) this unclosed term appearing in the Favre-averaged specie mass fraction equation is modeled as,

$$-\frac{\partial(\overline{\rho u'' Y''_{SF_6}})}{\partial x} \approx \frac{\partial(C_c \frac{S}{\sqrt{K}} \bar{\rho} \tilde{R}_{11} \frac{\partial(\tilde{Y}_{SF_6})}{\partial x})}{\partial x} \tag{7}$$

where Y_n is the mass fraction of n^{th} species. To test the validity of this modelling assumption, the quantity $-(\overline{\rho u''_j Y''_n})$ indicated as '**SO**' (second-order term) is plotted along with $(\bar{\rho}\tilde{R}_{jm}\tilde{Y}_{n,x}/\sqrt{K})$

(indicated as '**Model**') in Fig. 32. Results from the simulation on two different grid resolutions are presented. The agreement of slopes of these profiles would indicate validity of the model. It is seen that at early times and intermediate times before reshock the model does not capture the trend in the second-order quantity. Good agreement is obtained after reshock. This is expected because of the high degree of anisotropy existing in the flow field prior to reshock. Reshock provides additional energy in the already complex flow field to help transition to a turbulent flow where the gradient diffusion hypothesis is valid.

Similar analyses to the one presented above are conducted for unclosed terms appearing in other equations (Favre-averaged equations for turbulent mass flux, total energy and Reynolds stresses) and the corresponding details and results can be found in (26).

6.3 Richtmyer-Meshkov instability in spherical geometry

Lombardini et al. (22) have recently carried out Richtmyer-Meshkov instability (RMI) simulations in cylindrical geometry. RMI for a spherical axisymmetric flow was investigated by Dutta et al. (23). We consider a more general initial interface perturbation, with a spherical egg-carton profile similar to the one used in planar RMI simulations (19; 20). An interesting feature of this profile is that the perturbation wavelength is nearly constant over the spherical shell spanned by the material interface as seen in figure 33. The fluids considered in this study are air outside and SF_6 inside. The shock is launched from the air (lighter) side of the interface. As the flow evolves, a series of reflected and transmitted shocks are generated, which via baroclinic deposition of vorticity and its subsequent transport serve to mix the two fluids in a turbulent mixing zone.

To help elucidate the figures and discussion in the sections below, it is useful to define the different regimes of the flow. Three broad regimes can be identified. The first is the converging shock regime, when the shock is propagating inwards, not yet having reached the origin. The second is the reflected shock regime, when the shock has rebounded off of the origin, but is still within the simulation domain. The material interface is reshocked during this regime. The third regime is that of turbulent mixing, when the baroclinic vorticity deposited by the initial shock and reshock events, rises to a maximum and then decays as the two fluids mix.

These phases can be seen in slices of density and vorticity plotted in figures 34 and 35 where the left plot shows the converging phase of the flow and the right plot shows the reflected phase just after reshock and the turbulent mixing phase.

The mixing layer width is defined as $h = \int_{s=0}^{s=R_{max}} \langle Y \rangle (1 - \langle Y \rangle) ds$ where angled brackets $\langle . \rangle$ indicate a tangential average as a function of radius. Figure 36 compares mixing layer widths for the same initial perturbation, only the incident shock Mach number is varied. For all temporal profiles, time has been normalized with time taken for the shock to reach the origin so that the time of first shock and reshock are similar for all cases. Note that they cannot be identical, as in the planar case, because shock speed is a nonlinear function of time for a spherically converging shock. We also plot spatial profiles of $\langle Y \rangle (1 - \langle Y \rangle)$ for the $M_I = 1.8$ case which corroborates the trend observed in the temporal profiles.

The h profile has a shape similar to that observed in the planar case, with a slight initial drop as the incident shock compresses the perturbation, then a rise as the interface perturbation to grow into spikes and bubbles under the action of baroclinically deposited vorticity. The compression due to the reshock causes another drop in h, followed by a rise as the mixing layer grows in size and

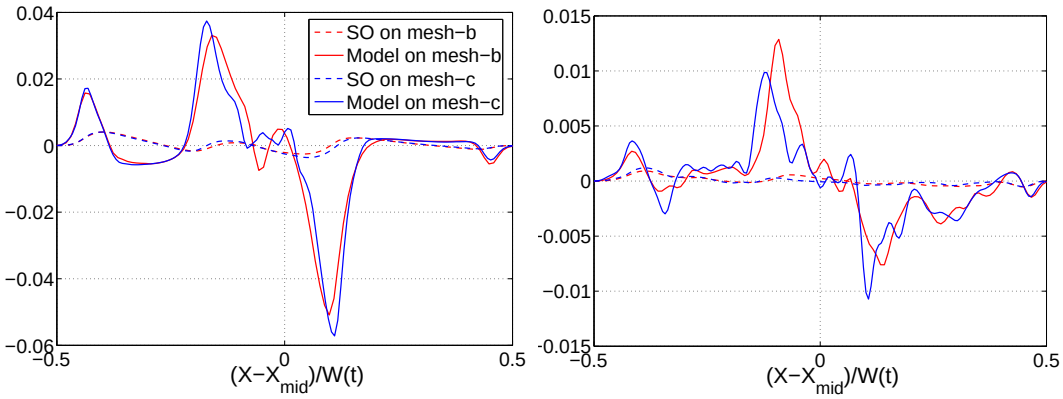

(a) t=277 μs

(b) t=571 μs

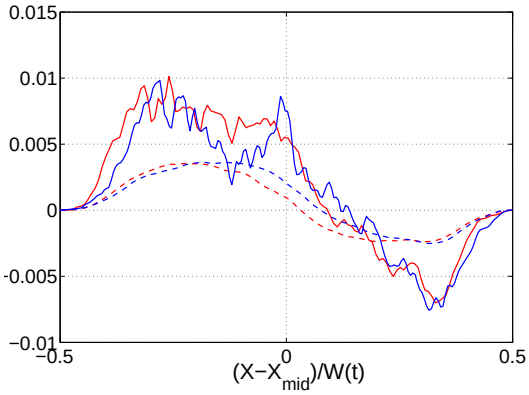

(c) t=733 μs

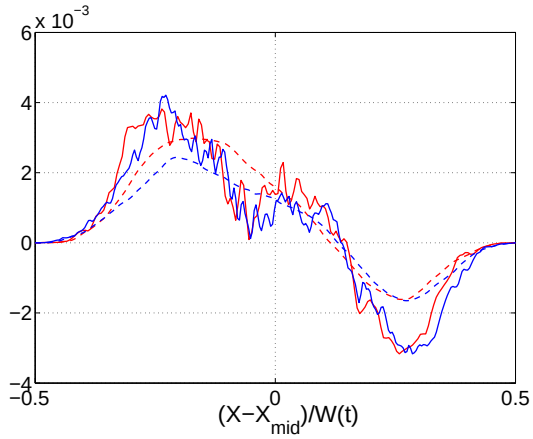

(d) t=855 μs

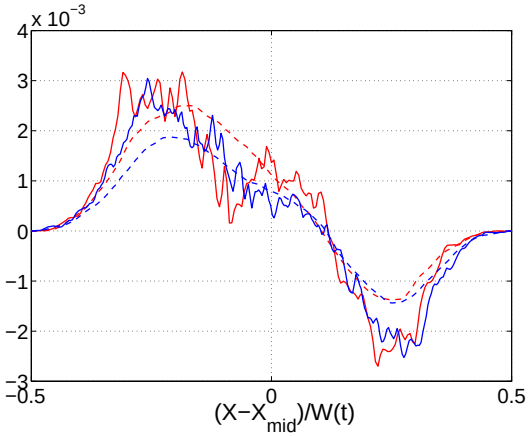

(e) t=906 μs

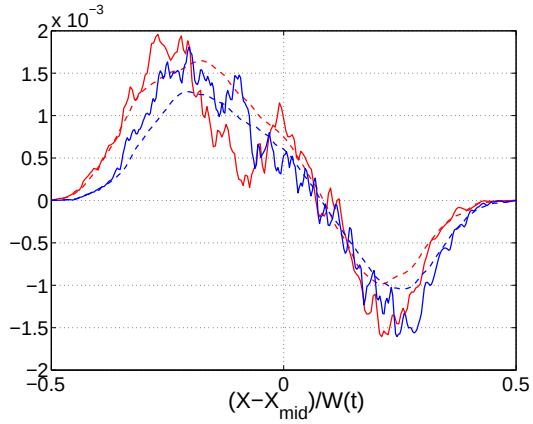

(f) t=1007 μs

Figure 32: Validity of modelling assumption based on gradient diffusion hypothesis to close the Favre-averaged specie mass fraction equation given by Eqn. 6. '**SO**' denotes the second order term appearing in the exact equation for species mass fraction (Eqn. 6) and '**Model**' denotes its modeled approximation (Eqn. 7).

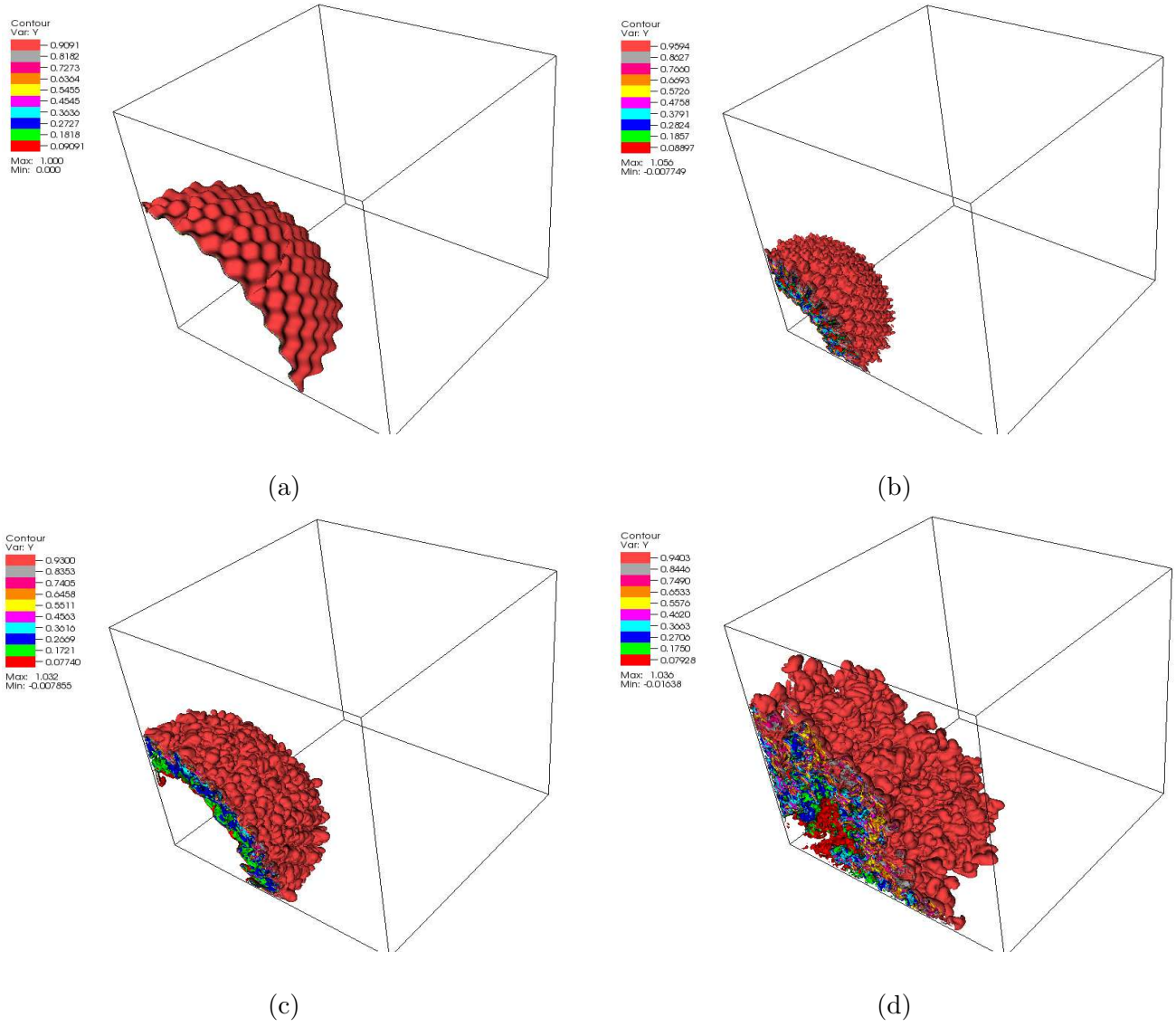

Figure 33: Evolution of spherical RMI for $M_I = 1.8$ and $k_0 = 32$. Contours of mass fraction, Converging shock regime: (a) $t/t_s = 0$, (b) $t/t_s = 0.8$. Post-reshock regime: $t/t_s = 2.4$, $t/t_s = 3.1$

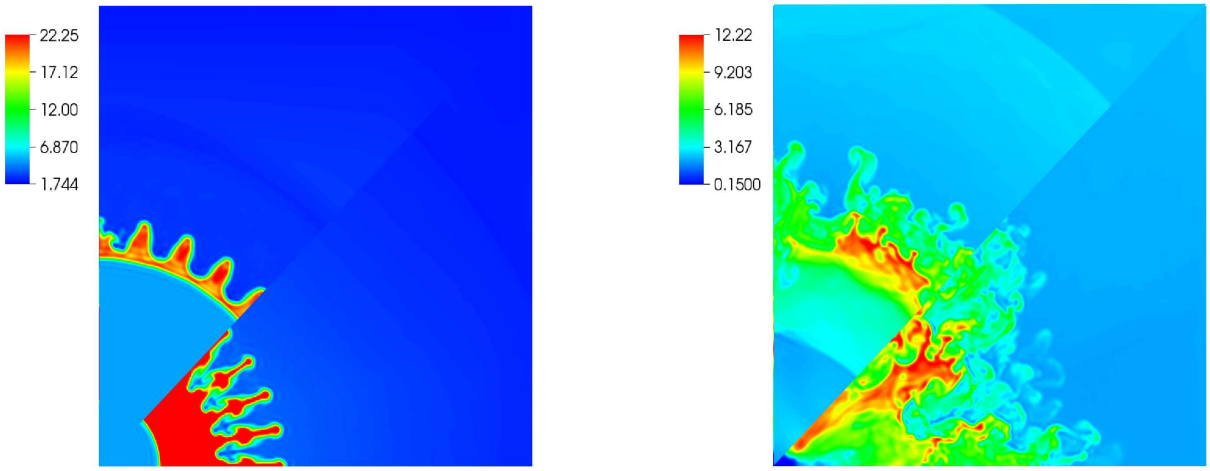

Figure 34: Evolution of spherical RMI for $M_I = 1.8$. Slices of density, $\rho/\rho_{air}^{unshocked}$ (a) Converging $t/t_s = 0.4$, $t/t_s = 0.8$, (b) Post-reshock regimes. $t/t_s = 2.4$, $t/t_s = 3.1$ Only half of the computed octant is shown.

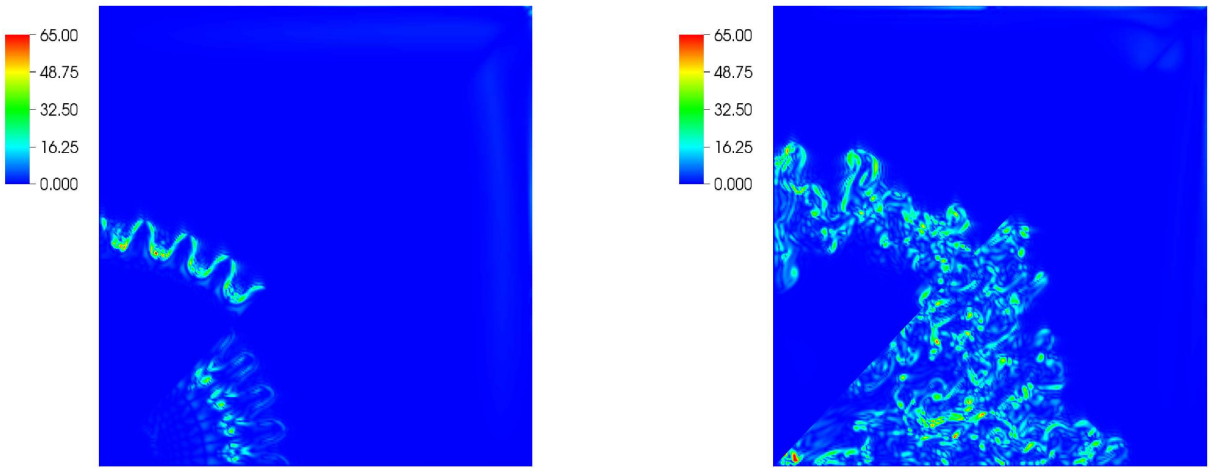

Figure 35: Evolution of spherical RMI for $M_I = 1.8$. Slices of density, $\rho/\rho_{air}^{unshocked}$ (a) Converging $t/t_s = 0.4$, $t/t_s = 0.8$, (b) Post-reshock regimes. $t/t_s = 2.4$, $t/t_s = 3.1$ Only half of the computed octant is shown.

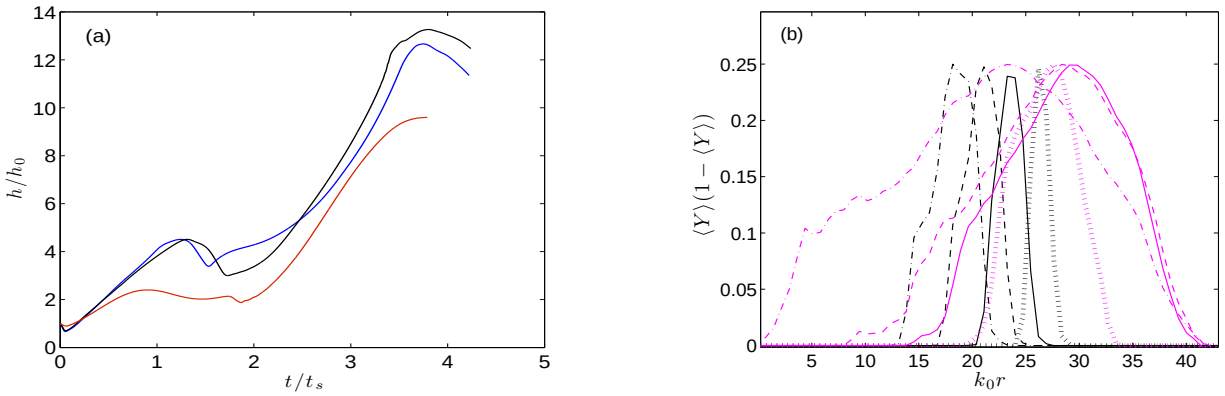

(a) (b)

Figure 36: (a) Comparison of mixing layer width. $M_I = 1.2$ (red), $M_I = 1.8$ (black), $M_I = 3.0$ (blue). Width normalized by initial perturbation amplitude. (b) Profiles of $\langle Y\rangle(1 - \langle Y\rangle)$ for $M_I = 1.8$ case, Converging (black) and post-reshock (magenta) phases. (a) Converging, $t/t_s = 0.2$ (dotted), $t/t_s = 0.36$ (solid), $t/t_s = 0.52$ (dashed), $t/t_s = 0.68$ (dash-dotted). (b) Post-reshock regimes, $t/t_s = 2.23$ (dotted), $t/t_s = 2.88$ (solid), $t/t_s = 3.1$ (dashed), $t/t_s = 3.74$ (dash-dotted). Y is the mass fraction of Air

becomes turbulent. The Mach number dependence is quite evident. In the linear growth phase, the profiles line up at early times, except for the lowest Mach number, which flattens out earlier. After reshock, peaks of the turbulent mixing layer widths occur at different times with the chosen time normalization. The shock speed based scaling of time therefore does not apply to the post reshock phase of the mixing layer growth. It is not clear that simple scaling parameters exist for this highly nonlinear process. The slope of the h/h_0 curve when evaluated against the scaled time is similar. This is an indication that the scale used in the plot captures an important dependence. Simulations at other Atwood numbers and interface perturbations are needed to judge if this is a robust scaling.

Figure 37 shows the evolution of domain integrated vorticity variance i.e enstrophy and perturbation kinetic energy, which eventually becomes turbulent kinetic energy (TKE) as the flow becomes turbulent. For ease of nomenclature, both are referred to as TKE in this paper. Similar to the planar case, it shows a double peak structure. The first rise and decay corresponds to the linear growth phase, while the second corresponds to the post-reshock turbulent mixing layer growth and eventual decay. Enstrophy is normalized by a time scale based on the initial velocity impulse to the interface by the incident shock, while TKE is normalized by shock speed. The vorticity profiles collapse quite well during the linear phase, but diverge at late times, when the flow is nonlinear and turbulent. The TKE profiles do not show such a good collapse, but the chosen normalization yields the best comparison between different cases.

7 Interactions, outreach and acknowledgments

A fundamental aspect of the SciDAC program is its collaborative nature. This SciDAC Application includes groups from several institutions: Stanford University, Lawrence Livermore National

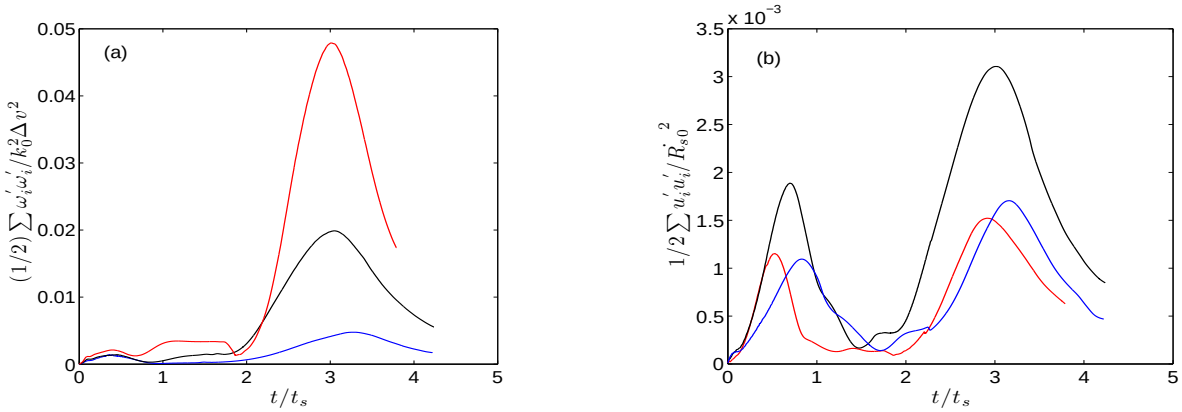

Figure 37: Comparison of Enstrophy and TKE. $M_I = 1.2$ (red), $M_I = 1.8$ (black), $M_I = 3.0$ (blue). (a) Enstrophy (b) TKE.

Laboratory, University of California Los Angeles and NASA Ames (through a SciDAC Science Application Partnership). Active collaborations have been maintained during this project with all its members. As an example, we cite the novel DNS of shock-turbulence interaction that Prof. Xiaolin Zhong, co-PI on our SciDAC Science Application team at UCLA, is conducting using shock-fitting algorithms. This new focus resulted from our collaborative work on comparative assessment of algorithms for shock-turbulence interaction problems, and became possible by re-directing some of Dr. Zhong's SAP effort for this science application.

Besides collaborations within the SciDAC context, several opportunities have arisen during the course of this work for external interactions with other members of the scientific community. These can be categorized into three types, based on the resources that are being shared: science, software and computer power.

Scientific collaborations include interactions with NASA Hypersonics and Supersonics projects, DOE PSAAP project at Stanford University on multi-physics simulations and uncertainty quantification for hypersonic vehicle and propulsion system flow, and the AFOSR-MURI project on inlets and scramjets combustors. We regularly organize *shocks meetings* to discuss work-in-progress related to high-speed flows, sharing new ideas and fostering collaborations among members of those projects. As already stated in this report, our DNS databases of shock-turbulence interaction have been shared with members of the PSAAP project, with scientists at TU Munich, Germany, and with scientists at Texas A&M University. We would like to acknowledge also valuable scientific exchanges with D. A. Donzis at Texas A&M University, B. J. Balakumar and K. Prestridge at Los Alamos National Laboratory, A. Cook, W. Cabot and B. Sjogreen at Lawrence Livermore National Laboratory, H. C. Yee at NASA Ames Research Center and X. Zhong at the University of California, Los Angeles.

Examples of software collaborations include our use of visualization tools, such as the VisIt software developed by VACET, and the optimization of our *Hybrid* code guided by the HPCToolkit software developed at Rice University, as directed by their Performance Engineering Research Institute. In addition, one of our graduate students completed a summer internship at Lawrence Berkeley National Laboratory working with a high-order adaptive mesh refinement code and applying it to simulations of shock-turbulence interaction.

The necessary use of supercomputers to carry out our numerical simulations has brought a continued collaboration with the DOE Leadership Computing program and the NCCS Early Access program. We have received valuable help from computer scientists at Lawrence Berkeley National Laboratory (NERSC), Oak Ridge National Laboratory and Argonne National Laboratory (ALCF). Reciprocally, our most demanding simulations performed at BG/P have helped to improve parallel I/O libraries developed at ANL for their application to large datasets. In the course of this SciDAC project we have received several Innovative and Novel Computational Impact on Theory and Experiment (INCITE) awards, allowing us to carry out the most computationally demanding numerical simulations.

8 Publications and presentations

Below is a list of the publications and presentations produced during the course of this project by the SciDAC team.

8.1 Journal Articles

A. Bhagatwala, S.K. Lele "Interaction of a converging spherical shock wave with isotropic turbulence." Phys. Fluids, 24, 085102 (2012)

J. Larsson, I. Bermejo-Moreno and S. K. Lele, "Reynolds- and Mach-number effects in canonical shock/turbulence interaction" *J. Fluid Mech.*, submitted (2012).

S.K. Shankar, S. Kawai, S.K. Lele, "Two-dimensional viscous flow simulation of a shock accelerated heavy gas cylinder", Phys. Fluids, 23, 5 (2011)

A. Bhagatwala, S.K. Lele "Interaction of a Taylor blast wave with isotropic turbulence." Phys. Fluids, 23, 035103 (2011)

J. Larsson, "Effect of shock-capturing errors on turbulence statistics" *AIAA J.* 49 (2010) 582–597.

E. Johnsen, J. Larsson, A. V. Bhagatwala, W. H. Cabot, P. Moin, B. J. Olson, P. S. Rawat, S. K. Shankar, B. Sjgreen, H. C. Yee, X. Zhong, and S. K. Lele, "Assessment of high resolution methods for numerical simulations of compressible turbulence", J. Comput. Phys. 229 (2010) 1213-1237.

S. Kawai, S. K. Shankar and S. K. Lele, "Assessment of localized artificial diffusivity scheme for large-eddy simulation of compressible turbulent flows", J. Comput. Phys., 229 (2010) 1739-1762.

M. Kupiainen and B. Sjogreen, "A Cartesian Embedded Boundary Method for the Compressible Navier- Stokes Equations", J. Scient. Comput. 41 (2009) 94-117.

A. Mani, J. Larsson and P. Moin, "Suitability of artificial bulk viscosity for large-eddy simulation of turbulent flows with shocks", J. Comput. Phys. 228 (2009) 7368-7374.

J. Larsson and S. K. Lele, "Direct numerical simulation of canonical shock/turbulence interaction", Phys. Fluids 21, 126101 (2009). [0]

W. Wang, C. W. Shu, H. C. Yee and B. Sjgreen, "High order well-balanced schemes and applications to non-equilibrium flow with stiff source terms", J. Comput. Phys. 228 (2009) 6682-6702.

A. Bhagatwala and S. K. Lele, "A modified artificial viscosity approach for compressible turbulence simulations", J. Comput. Phys. 228 (2009) 4965-4969.

B. Sjgreen and H. C. Yee, "Variable High Order Multiblock Overlapping Grid Methods for Mixed Steady and Unsteady Multiscale Viscous Flows", Commun. Comput. Phys. 5 (2009) 730-744.

J. Larsson, "Blending technique for compressible inflow turbulence: algorithm localization and accuracy assessment", J. Comput. Phys. 228 (2009) 933-937.

J. Larsson and B. Gustafsson, "Stability criteria for hybrid difference methods", J. Comput. Phys. 227 (2008) 2886–2898.

8.2 Conference Proceedings

S.K. Shankar, S. Kawai, S.K Lele, "Numerical simulation of multicomponent shock accelerated flows and mixing using localized artificial diffusivity method", 48^{th} AIAA Aerospace Sciences Meeting 352.

E. Johnsen and J. Larsson, "A low-dissipation method for DNS of compressible turbulent multicomponent and multiphase flows with shocks" 7th International Conference on Multiphase Flow, ICMF 2010, Tampa, FL, May 30 – June 4, 2010

S. Hickel and J. Larsson, "On implicit turbulence modeling for LES of compressible flows", in *Advances in Turbulence XII*, B. Eckhardt (Ed.), Springer, 2009.

S. Chumakov and J. Larsson, "Lag-modeling of subgrid-scale dissipation in large eddy simulation", in *Turbulent Mixing and Beyond*, 2009.

S.K. Lele and J. Larsson, "Shock-turbulence interaction: What we know and what we can learn from peta-scale simulations", *J. Phys.: Conf. Ser.* 180, 012032, 2009.

J. Larsson and S. K. Lele, "Direct numerical simulations of canonical shock/turbulence interaction", Sixth International Symposium on Turbulence and Shear Flow Phenomena, June 22-24, 2009, Seoul, Korea.

S. Kawai, S. K. Shankar, "LES of compressible turbulent flows: assessment of compact differencing with localized artificial diffusivity scheme", AIAA paper 2009-1505, 2009.

P. Rawat and X. Zhong, "High-Order Shock-Fitting and Front-Tracking Methods for Numerical Simulation of Shock- Disturbance Interactions", AIAA paper 2009-1138, 2009.

8.3 Presentations

A. Bhagatwala and Lele, S., "Shock Turbulence Interaction In Spherical Geometry, Thermal and Fluid Science Aliates Conference, Stanford University, Stanford, California, February 2011.

S. Shankar and Lele, S., "LES of Multi-material Shock Induced Mixing, Thermal and Fluid Science Aliates Conference, Stanford University, Stanford, California, February 2011.

I. Bermejo-Moreno, Larsson, J. and Lele, S., "Large-eddy simulations of the shock-turbulence interaction canonical problem, Thermal and Fluid Science Aliates Conference, Stanford University, Stanford, California, February 2011.

S. K. Shankar and S. K. Lele, "Sensitivity of Shock Accelerated Multi-Component Compressible Flows" 63rd Annual Meeting of the APS Division of Fluid Dynamics, Long Beach, California, November 21-23, 2010

I. Bermejo-Moreno, J. Larsson and S. K. Lele, "Large-eddy simulations of the shock-turbulence interaction canonical problem" 63rd Annual Meeting of the APS Division of Fluid Dynamics, Long Beach, California, November 21-23, 2010

S. K. Lele and J. Larsson, "Shock/turbulence interaction", Tutorial during the 85-person strong 2010 Stanford Summer Program on Turbulence.

A. Bhagatwala and S. Lele "Shock-turbulence interactions in spherical geometry" Thermal and Fluid Sciences Affiliates and Sponsors Conference, Stanford, CA, February 3-5, 2010.

S. Shankar and S. Lele "Mixing in multi-component shock-accelerated flows using localized artificial diffusivity method" Thermal and Fluid Sciences Affiliates and Sponsors Conference, Stanford, CA, February 3-5, 2010.

B. Sjogreen, 4th International Conference on Numerical Modeling of Space Plasma Flows (ASTRONUM-2009), Chamonix, France, June 28 - July 3, 2009.

H. C. Yee, 4th International Conference on Numerical Modeling of Space Plasma Flows (ASTRONUM-2009), Chamonix, France, June 28 - July 3, 2009.

H. C. Yee and B. Sjogreen, International Conference on Spectral and High Order Methods (ICOSAHOM-2009), Trondheim, Norway, June 22-26, 2009.

H. C. Yee and B. Sjogreen, "High Order Methods of Turbulence with Strong Shocks", 8th European Conference on Numerical Mathematics and Advanced Applications (ENUMATH-2009), June 29 -

July 3, 2009, Uppsala University, Sweden.

S. K. Lele, SciDAC 2009 conference, San Diego, CA, June 14-18, 2009.
J. Larsson, and S. K. Lele, Sixth International Symposium on Turbulence and Shear Flow Phenomena, Seoul, Korea, June 2009.

9 Personnel supported and unexpended funds

In this section we list the personnel that has been supported (at least in part) throughout the SciDAC project at Stanford University:

- Prof. Sanjiva Lele – PI
- Prof. Parviz Moin – Co-PI
- Prof. Chi-Wang Su – Senior Visiting Fellow
- Dr. Johan Larsson – Research Associate
- Dr. Eric Johnsen – Post-doctoral fellow
- Dr. Wei Wang – Post-doctoral fellow
- Dr. Iván Bermejo-Moreno – Post-doctoral fellow
- Mr. Ankit Bhagatwala – Graduate student
- Mr. Santhosh Shankar – Graduate student
- Mr. Britton Olson – Graduate student
- Mr. Rathakrishnan Bhaskaran – In part graduate student
- Mr. Jin-Woo Lee – In part graduate student

References

[1] H. S. Ribner, Shock-turbulence interaction and the generation of noise, NACA Report 1233, NACA (1954).

[2] S. Lee, S. K. Lele, P. Moin, Interaction of isotropic turbulence with shock waves: effect of shock strength, J. Fluid Mech. 340 (1997) 225–247.

[3] J. Larsson, S. K. Lele, Direct numerical simulation of canonical shock/turbulence interaction, Phys. Fluids 21 (2009) 126101.

[4] Larsson, J. & Lele, S. K. 2009 Direct numerical simulation of canonical shock/turbulence interaction. *Phys. Fluids* **21**, 126101.

[5] Bermejo-Moreno, I. 2009 Subgrid-scale modeling of shock-turbulence interaction for large-eddy simulations. In *Annu. Res. Briefs, Center for Turbulence Research*, pp. 247–259.

[6] Ducros, F., Laporte, F., Souleres, T. & Guinot, V. 2000 High-order fluxes for conservative skew-symmetric-like schemes in structures meshes: Application to compressible flows. *J. Comput. Phys.* **161**, 114.

[7] Smagorinsky, J. 1963 General circulation experiments with the primitive equations 1. the basic experiment. *Mon. Weather Rev.* **91**, 99–164.

[8] A. W. Vreman, An eddy-viscosity subgrid-scale model for turbulent shear flow: Algebraic theory and applications, Phys. Fluids 16 (10) (2004) 3670–3681.

[9] M. Germano, U. Piomelli, P. Moin, W. H. Cabot, A dynamic subgrid-scale eddy viscosity model, Phys. Fluids A 3 (1991) 1760–1765.

[10] D. K. Lilly, A proposed modification of the Germano subgrid-scale closure method, Phys. Fluids A 4 (3) (1992) 633–635.

[11] C. Meneveau, T. S. Lund, W. H. Cabot, A Lagrangian dynamic subgrid-scale model of turbulence, J. Fluid Mech. 319 (1996) 353–385.

[12] A. Misra, D. I. Pullin, A vortex-based subgrid stress model for large-eddy simulation, Phys. Fluids 9 (1997) 2443–2454.

[13] B. Kosovic, D. I. Pullin, R. Samtaney, Subgrid-scale modeling for large-eddy simulations of compressible turbulence, Phys. Fluids 14 (2002) 1511–1522.

[14] Lundgren, T. S. 1982 Strained spiral vortex model for turbulent fine structure. *Phys. Fluids* **12**, 2193.

[15] D. I. Pullin, A vortex-based model for the subgrid flux of a passive scalar, Phys. Fluids 12 (2000) 2311–2319.

[16] Larsson, J. 2010 Effect of shock-capturing errors on turbulence statistics. *AIAA J.* **48(7)**, 1554–1557.

[17] A.W. Cook "Artificial Fluid properties for Large-Eddy Simulation of Compressible turbulent mixing." *Phys. Fluids*, 19, 055103 (2007)

[18] A. Bhagatwala, S.K. Lele "Interaction of a Taylor blast wave with isotropic turbulence." *Phys. Fluids*, 23, 035103 (2011)

[19] M. Vetter, B. Sturtevant, Experiments on the Richtmyer-Meshkov instability of an air/sf6 interface, Shock Waves 4 (1995) 247–252.

[20] D. J. Hill, C. Pantano, D. I. Pullin, Large-eddy simulation and multiscale modelling of a Richtmyer-Meshkov instability with reshock, J. Fluid Mech. 557 (2006) 26–61.

[21] B. J. Balakumar, G. C. Orlicz, C. D. Tomkins, K. P. Prestridge, Simultaneous particle-image velocimetry–planar laser-induced fluorescence measurements of Richtmyer-Meshkov instability growth in a gas curtain with and without reshock, Phys. Fluids 20 (2008) 124103.

[22] Lombardini M., Deiterding R., Pullin D. I. Large Eddy Simulations of the RichtmyerMeshkov Instability in a Converging Geometry. *Quality and Reliability of Large-Eddy Simulations*, 283-294 (2008)

[23] Dutta S., Glimm J., Grove J.W., Sharp D.H., Zhang Y. Spherical Richtmyer-Meshkov instability for axisymmetric flow. *Mathematics and Computers in Simulation*, 65, 417 (2004)

[24] S.K. Shankar, S. Kawai, S.K. Lele, Two-dimensional viscous flow simulation of a shock accelerated heavy gas cylinder, Phys. of Fluids **23**,5 (2011)

[25] J.D. Schwarzkopf, D. Livescu, R.A. Gore, R.M. Rauenzahn, and J.R. Ristorcelli. Application of a second-moment closure model to mixing processes involving multicomponent miscible fluids. *Journal of Turbulence*, 12(N49) (2011).

[26] S. Shankar, Numerical investigation of turbulence and mixing in shock-accelerated multicomponent compressible flows", Ph.D. thesis, Stanford University (2012)

[27] N. A. Adams, K. Shariff, A high-resolution hybrid compact-ENO scheme for shock-turbulence interaction problems, J. Comput. Phys. 127 (1996) 27–51.

[28] M. Arora, P. L. Roe, On postshock oscillations due to shock capturing schemes in unsteady flows, J. Comput. Phys. 130 (1997) 25–40.

[29] A. V. Bhagatwala, S. K. Lele, A modified artificial nonlinear viscosity approach for compressible turbulence simulations, J. Comput. Phys. 228 (2009) 4965–4969.

[30] M. E. Brachet, D. I. Meiron, S. A. Orszag, B. G. Nickel, R. H. Morf, U. Frisch, Small-scale structure of the Taylor-Green vortex, J. Fluid Mech. 130 (1983) 411–452.

[31] W. Cheney and D. Kincaid, Numerical Mathematics and Computing, 4th Ed. Brooks/Cole Thomson Learning, Belmont, CA (2004).

[32] A. W. Cook, W. H. Cabot, A high-wavenumber viscosity for high-resolution numerical methods, J. Comput. Phys. 195 (2004) 594–601.

[33] A. W. Cook, W. H. Cabot, Hyperviscosity for shock-turbulence interactions, J. Comput. Phys. 203 (2005) 379–385.

[34] A. W. Cook, J. Larsson, W. H. Cabot, S. K. Lele, Simulation strategies for shock-turbulence interactions, Proceedings of the 7th International Symposium on Engineering Turbulence Modelling and Measurements, European Research Collaboration on Flow Turbulence and Combustion, Limassol, Cyprus (2008).

[35] X. Deng, H. Zhang, Developing high-order weighted compact nonlinear schemes, J. Comput. Phys. 203 (2005) 22–44.

[36] F. Ducros, V. Ferrand, F. Nicoud, C. Weber, D. Darracq, C. Gacherieu, T. Poinsot, Large-eddy simulation of the shock/turbulence interaction, J. Comput. Phys. 152 (1999) 517–549.

[37] F. Ducros, F. Laporte, T. Souleres, V. Guinot, P. Moinat, B. Caruelle, High-order fluxes for conservative skew-symmetric-like schemes in structured meshes: application to compressible flows, J. Comput. Phys. 161 (2000) 114–139.

[38] B. Fiorina, S. K. Lele, An artificial nonlinear diffusivity method for supersonic reacting flows with shocks, J. Comput. Phys. 222 (2007) 246–264.

[39] D. V. Gaitonde, M. R. Visbal, High-order schemes for Navier-Stokes equations: algorithm and implementation into FDL3DI, Tech. Rep. AFRL-TR-98, U.S. Air Force Research Lab. (1998).

[40] E. Garnier, M. Mossi, P. Sagaut, P. Comte, M. Deville, On the use of shock-capturing schemes for large-eddy simulations, J. Comput. Phys. 153 (1999) 273–311.

[41] J. A. Greenough and W. J. Rider, A quantitative comparison of numerical methods for the compressible Euler equations: fifth-order WENO and piecewise-linear Godunov, J. Comput. Phys. 196 (2004) 259–281.

[42] M. Hahn, D. Drikakis, Large eddy simulation of compressible turbulence using high-resolution methods, Int. J. Num. Meth. Fluids 47 (2005) 971–977.

[43] D. J. Hill, D. I. Pullin, Hybrid tuned center-difference-WENO method for large eddy simulations in the presence of strong shocks, J. Comput. Phys. 194 (2004) 435–450.

[44] F. Q. Hu, M. Y. Hussaini, and J. L. Manthey, Low-dissipation and low-dispersion Runge-Kutta schemes for computational acoustics, J. Comput. Phys. 124 (1996) 177–191.

[45] A. Jameson, W. Schmidt, E. Turkel, Numerical simulation of the Euler equations by finite volume methods using Runge-Kutta time stepping schemes, AIAA 5th Computations Fluid Dynamics Conference (1981).

[46] G. S. Jiang, C. W. Shu, Efficient implementation of weighted ENO schemes, J. Comput. Phys. 126 (1996) 202–228.

[47] S. Kawai, S. K. Lele, Localized artificial diffusivity scheme for discontinuity capturing on curvilinear meshes, J. Comput. Phys. 227 (2008) 9498–9526.

[48] S. Kawai, S. K. Shankar, S. K. Lele, Assessment of localized artificial diffusivity scheme for large-eddy simulation of compressible turbulent flows, J. Comput. Phys. (2009)

[49] B. Kosovic, D. I. Pullin, R. Samtaney, Subgrid-scale modeling for large-eddy simulations of compressible turbulence, Phys. Fluids 14 (2002) 1511–1522.

[50] J. Larsson, B. Gustafsson, Stability criteria for hybrid difference methods 227 (2008), 2886–2898.

[51] J. Larsson, S. K. Lele, P. Moin, Effect of numerical dissipation on the predicted spectra for compressible turbulence, Tech. Rep. Ann. Res. Briefs, Center for Turbulence Research, Stanford University (2007).

[52] S. Lee, S. K. Lele, P. Moin, Eddy shocklets in decaying compressible turbulence, Phys. Fluids 3 (1991) 657–664.

[53] R. J. LeVeque, Finite volume methods for hyperbolic problems, Cambridge University Press, Cambridge, UK (2002).

[54] R. Liska, B. Wendroff, Comparison of several difference schemes on 1D and 2D test problems for the Euler equations, SIAM J. Sci. Comput. 25 (2003) 995–1017.

[55] C. Lui, S. K. Lele, Direct numerical simulation of spatially developing, compressible, turbulent mixing layers, AIAA-2001-0291, 2001.

[56] K. Mahesh, The interaction of a shock wave with a turbulent shear flow, Ph.D. thesis, Stanford University (2000).

[57] A. Mani, J. Larsson, P. Moin, Suitability of bulk viscosity for large-eddy simulation of turbulent flows with shocks, J. Comput. Phys. 228 (2009) 7368–7374.

[58] M. P. Martin, E. M. Taylor, M. Wu, V. G. Weirs, A bandwidth-optimized WENO scheme for the effective direct numerical simulation of compressible turbulence, J. Comput. Phys. 220 (2006) 270–289.

[59] W. F. Noh, Errors for calculations of strong shocks using an artificial viscosity and an artificial heat flux, J. Comput. Phys. 72 (1978) 78–120.

[60] S. Pirozzoli, Conservative hybrid compact-WENO schemes for shock-turbulence interaction, J. Comput. Phys. 178 (2002) 81–117.

[61] J. R. Ristorcelli, G. A. Blaisdell, Consistent initial conditions for the DNS of compressible turbulence Phys. Fluids 9 (1997) 4–6.

[62] R. Sanders, E. Morano, M. C. Druguet, Multidimensional dissipation for upwind schemes: stability and applications to gas dynamics, J. Comput. Phys. 145 (1998) 511–537.

[63] J. V. Shebalin, Pseudospectral simulation of compressible turbulence using logarithmic variables, AIAA-93-3375-CP, (1993).

[64] C. W. Shu, S. Osher, Efficient implementation of essentially non-oscillatory shock capturing schemes II, J. Comput. Phys. 93 (1989) 32–78.

[65] C. W. Shu, Essentially non-oscillatory and weighted essentially non-oscillatory schemes for hyperbolic conservation laws, ICASE Report No. 97-65, NASA Langley Research Center (1997).

[66] B. Sjögreen, H. C. Yee, Multiresolution wavelet based adaptive numerical dissipation control for high order methods, J. Scient. Comput. 20 (2004) 211–255.

[67] B. Sjögreen, H. C. Yee, Skew symmetric splitting for the gas dynamics equations, Proceedings of the eighth European Conference on Numerical Mathematics and Advanced Applications, Uppsala, Sweden (2009) in press.

[68] D. Stanescu and W. G. Habashi, $2N$-storage low dissipation and dispersion Runge-Kutta schemes for computational acoustics, J. Comput. Phys. 143 (1998) 674–681.

[69] G. I. Taylor, A. E. Green, Mechanism of the production of small eddies from large ones, Proc. R. Soc. Lond. A 158 (1937) 499–521.

[70] E. F. Toro, Riemann solvers and numerical methods for fluid dynamics, Springer-Verlag, Heidelberg, Germany (1999).

[71] M. R. Visbal, D. V. Gaitonde, Shock capturing using compact-differencing-based methods, AIAA-2005-1265, 2005.

[72] P. Woodward, P. Colella, The numerical simulation of two-dimensional fluid flow with strong shocks, J. Comput. Phys. 54 (1984) 115–173.

[73] H. C. Yee, N. D. Sandham, M. J. Djomehri, Low-dissipative high-order shock-capturing methods using characteristic-based filters, J. Comput. Phys. 150 (1999) 199–238.

[74] H. C. Yee, M. Vinokur, M. J. Djomehri, Entropy splitting and numerical dissipation, J. Comput. Phys. 162 (2000) 33–81.

[75] H. C. Yee, B. Sjögreen, Development of low dissipative high-order filter schemes for multiscale Navier-Stokes/MHD systems, J. Comput. Phys. 225 (2007) 910–934.

[76] H. C. Yee, B. Sjögreen, Adaptive filtering and limiting in compact high order methods for multiscale gas dynamics and MHD systems, Comput. Fluids 37 (2008) 593–619.

[77] X. Zhong, High-order finite-difference schemes for numerical simulation of hypersonic boundary-layer transition, J. Comput. Phys. 144 (1998) 662–709.

[78] Barre, S., Alem, D. & Bonnet, J. P. 1996 Experimental study of a normal shock/homogeneous turbulence interaction. *AIAA J.* **34** (5), 968–974.

[79] Sinha, K., Mahesh, K. & Candler, G. V. 2003 Modeling shock unsteadiness in shock/turbulence interaction. *Phys. Fluids* **15** (8), 2290–2297.